Moisture Transport, Lower-Tropospheric Stability, and Decoupling of Cloud-Topped Boundary Layers

CHRISTOPHER S. BRETHERTON AND MATTHEW C. WYANT

Department of Atmospheric Sciences, University of Washington, Seattle, Washington

(Manuscript received 8 November 1995, in final form 26 June 1996)

ABSTRACT

Decoupling during the ''Lagrangian'' evolution of a cloud-topped boundary layer advected equatorward by the trade winds in an idealized eastern subtropical ocean is studied using a mixed-layer model (MLM). The sea surface temperature is gradually warmed while the free tropospheric sounding remains unchanged, causing the boundary layer to deepen, the surface relative humidity to decrease, and surface latent heat fluxes to increase. Diurnally averaged insolation is used.

For entrainment closures in which entrainment rate is related to a large-eddy convective velocity scale w^*, the MLM predicts an increasingly prominent layer of negative buoyancy fluxes below cloud base as the sea surface temperature warms. Decoupling of the mixed layer can be inferred when the MLM-predicted negative buoyancy fluxes become too large for the internal circulations to sustain. The authors show that decoupling is mainly driven by an increasing ratio of the surface latent heat flux to the net radiative cooling in the cloud, and derive a decoupling criterion based on this ratio. Other effects such as drizzle, the vertical distribution of radiative cooling in the cloud, and sensible heat fluxes, also affect decoupling but are shown to be less important in typical subtropical boundary layers. A comparison of MLM results with a companion numerical study with a cloud-resolving model shows that the decoupling process is similar and the same decoupling criterion applies. A regional analysis of decoupling using Lagrangian trajectories based on summertime northeast Pacific climatology predicts decoupling throughout the subtropical stratocumulus region except in coastal zones where the boundary layer is under 750 m deep.

A ''flux-partitioning'' entrainment closure, in which the entrainment rate is chosen to maintain a specified ratio of some measure of negative subcloud buoyancy fluxes to positive buoyancy fluxes within the cloud and near the surface, was also considered. By construction, such an MLM never predicts its own breakdown by decoupling. The changed entrainment closure had only a minor influence on the boundary layer evolution and entrainment rate. Instead, the crucial impact of the entrainment closure is on predicting when and where the mixed-layer assumption will break down due to decoupling.

1. Introduction

Much of our knowledge of subtropical marine stratocumulus cloud-topped boundary layers (CTBLs) comes from field experiments off the California coast, where the marine inversion is strong and typically between 400 and 800 m deep. These experiments showed that such CTBLs are well mixed by turbulence that is usually driven by radiative cooling at cloud top (Lilly 1968). The FIRE (First International Satellite Cloud Climatology Project Regional Experiment) marine stratocumulus experiment (Albrecht et al. 1988) also showed that daytime absorption of solar radiation in the clouds often leads to afternoon cloud thinning due to diurnal decoupling. Decoupling can occur when subcloud buoyancy fluxes become negative, inhibiting convection below cloud base. A stable layer develops there, separating a layer of surface-flux driven turbulence beneath from radiatively driven convection in the cloud layer. Cumulus clouds may form at the top of the surface mixed layer and rise through the stable layer, initiating a new form of dynamical organization within the boundary layer. Bulk model and turbulence closure models reproduce the diurnal cycle quite well (Bougeault 1985; Turton and Nicholls 1987; Duynkerke 1993). These models show that diurnal decoupling occurs because of the large negative buoyancy fluxes below cloud base necessary to maintain a mixed layer while solar absorption heats the cloud.

Convectively driven CTBLs are uniquely vulnerable to decoupling because unlike in the dry boundary layer, buoyancy flux (the prime source of their turbulent kinetic energy) is not a linear function of height. Instead there is a large increase in buoyancy flux above cloud base, proportional to the upward transport of liquid water in the CTBL that is required to sustain the cloud against entrainment drying [see Schubert et al. (1979)

Corresponding author address: Christopher S. Bretherton, University of Washington, Department of Atmospheric Sciences, Box 351640, Seattle, WA 98195-1640.
E-mail: breth@atmos.washington.edu

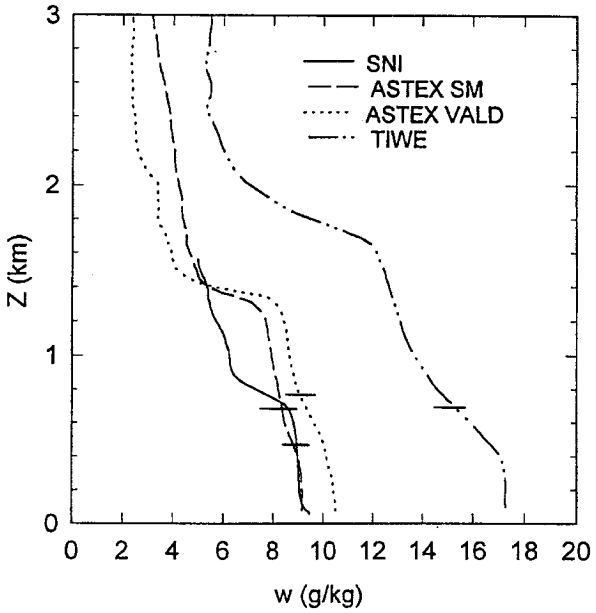

FIG. 1. Composite soundings of mixing ratio from four marine locations, SNI (San Nicolas Island, 30 June–19 July 1987, 33°N, 120°W, SST = 289 K, cloud fraction = 0.83); ASTEX SM (Santa Maria Island, 1–30 June 1992, 37°N, 25°W, SST = 291 K, CF = 0.67); ASTEX VALD (R/V *Valdivia*, 2–15 June 1992, 28°N, 24°W, SST = 294 K, CF = 0.40); and TIWE (R/V *Moana Wave*, 21 November–13 December 1991, 0°N, 140°W, SST = 300 K, CF = 0.26), from Albrecht et al. (1995b).

for a physical explanation of this fundamental point]. Large in-cloud liquid water fluxes concentrate convective energy generation within the cloud layer and often create an internal minimum of buoyancy flux below cloud base, setting the stage for decoupling.

If the Bowen ratio is small, as is typical of subtropical CTBLs, the liquid water flux in the cloud layer is proportional to the upward moisture or latent heat flux. Thus, a larger latent heat flux promotes decoupling even without the help of solar absorption. A similar conclusion was reached by Lewellen et al. (1996) from numerical simulations of shallow stratocumulus layers subject to prescribed surface fluxes. In this paper, we suggest that surface latent heat fluxes are the most important determinant of decoupling for subtropical CTBLs.

Climatologies of Neiburger (1960) and Betts et al. (1992) show that a large fraction of the area usually covered by subtropical stratocumulus cloud lies well off the coast where the inversion is typically 1–2 km deep. The Atlantic Stratocumulus Transition Experiment or ASTEX (Albrecht et al. 1995a) off the Azores Islands in the central Atlantic Ocean studied such deeper boundary layers. Their vertical structure is far from well mixed, even at night. A moist surface layer feeds cumulus clouds, which rise through a drier layer above and detrain into a thin and often patchy stratocumulus layer beneath the trade inversion. Figure 1 from Albrecht et al. (1995b) shows the climatological vertical moisture structure of four CTBLs during three field experiments. When the SST is relatively cold and lower tropospheric stability (Klein and Hartmann 1993) is high (SNI profile), the CTBL is shallow and relatively well mixed. Deeper boundary layers with more pronounced internal moisture gradients predominate where SST's are warmer (decreased lower tropospheric stability). The ASTEX SM (Santa Maria) profile shows that the cloud fraction of climatologically decoupled CTBLs can be 67% or more but that, over warmer SSTs, cloud fraction decreases.

Two-dimensional eddy-resolving model (ERM) simulations of the ''Lagrangian'' evolution of a column of CTBL air as it is advected equatorward over warmer water (Krueger et al. 1995; Wyant et al. 1996) show a similar change in vertical structure as the SST warms and the boundary layer deepens. In these simulations, the sounding above the boundary layer does not change and diurnally averaged insolation is used. If a diurnal cycle is included, it modulates but does not qualitatively change the CTBL evolution. When the SST is cold, the CTBL is shallow and well mixed. As the SST warms and the CTBL deepens, the lifted condensation levels in the updrafts and downdrafts gradually begin to separate, signifying that the boundary layer is becoming less well mixed and that the cloud layer is becoming drier than the subcloud layer. We call this ''deepening-warming'' decoupling. As the separation of updraft and downdraft lifted condensation level (LCL) increases, the updrafts take on the character of small cumulus clouds detraining into an upper stratocumulus layer—a ''cumulus-coupled'' CTBL.

Wyant et al. (1997, hereafter W97), show that deepening-warming decoupling, like diurnal decoupling, is preceded by increasingly negative buoyancy fluxes below cloudbase. These simulations show that decoupling is a crucial first step in the transition from shallow stratocumulus to trade cumulus in the subtropics, but (as also seen in Fig. 1) it does not immediately lead to a drop in stratocumulus cloud amount. Large areas of the eastern subtropical oceans appear to be covered by cumulus-coupled CTBLs (Klein et al. 1995). In the days after decoupling, the cumulus layer gradually deepens and the cumuli become more energetic. Penetrative entrainment of dry and warm free tropospheric air by the cumuli evaporates most of the liquid water in their updrafts before it can be detrained as stratocumulus cloud, so cloud amount gradually decreases (Bretherton 1992; W97).

This paper aims to give a satisfying dynamical explanation of what causes deepening-warming decoupling and to identify parameters that control when a CTBL will decouple without the help of the diurnal cycle. We draw from the Turton and Nicholls (1987) study of diurnal decoupling, hereafter TN87. We use the buoyancy flux profile produced by a mixed-layer model (MLM) of the CTBL to diagnose when decou-

pling can be expected. Section 2 describes the MLM, discusses a control run illustrating deepening-warming decoupling, and addresses the sensitivity of the results to the entrainment closure. In section 3, a discussion of the energy balance of the cloud layer is used to explain why many features of the boundary-layer evolution are insensitive to the entrainment closure, yet the existence and timing of decoupling is sensitive to the entrainment closure. In section 4, we derive a ''flux ratio'' criterion for decoupling involving the radiative flux divergence integrated across the cloud layer, the surface latent heat flux, the cloud thickness, and the vertical profile of drizzle. In section 5, we compare our MLM results and flux-ratio decoupling criterion with W97's eddy-resolving model of CTBL evolution, which was run using the same environmental conditions. In section 6, we drive the MLM with summertime northeastern Pacific Ocean climatology to predict where the decoupling transition typically occurs. Section 7 presents the conclusions.

2. Mixed-layer model diagnosis of decoupling induced by increasing SST

a. Mixed-layer model description

The MLM is formulated in terms of two thermodynamic quantities, both of which are assumed to be conserved in adiabatic motions of a moist air parcel. The total water mixing ratio $q_t = q_v + q_l$ is the sum of the water vapor and (where the air is saturated) the cloud liquid water mixing ratio. The moist static energy $h = C_pT + gz + Lq_v$, where T and z are temperature and height and C_p and L are the isobaric heat capacity of dry air and latent heat of vaporization for water vapor.

The MLM includes parameterizations of surface fluxes, drizzle, long- and shortwave radiation, and subsidence. The environmental parameters that must be specified at all times include sea surface temperature (SST), 10-m wind speed V, a height-independent horizontal divergence D, profiles of moist static energy $h^+(z)$, water vapor mixing ratio $q_t^+(z)$ above the CTBL, and a water vapor path above the domain top (for specifying downwelling longwave radiation). The MLM is generally similar to TN87's, but to be compatible with the two-stream radiation scheme used in W97 the radiative and drizzle fluxes are computed on a fixed set of gridpoints, while TN87 used grid levels that moved with the predicted inversion and cloud base. Careful discretization of the vertical integral of buoyancy flux ensures that cloud base and top evolve smoothly between grid points.

The MLM prognostic equations for the inversion height z_i, the mixed-layer total water mixing ratio q_{tM}, and the mixed-layer moist static energy h_M are

$$dz_i/dt = w_e - Dz_i, \tag{1}$$

$$dh_M/dt = -\partial E/\partial z,$$

$$E(z) = \{\langle w'h'\rangle + F_R/\rho_{\text{ref}}\}, \tag{2}$$

$$dq_{tM}/dt = -\partial W/\partial z,$$

$$W(z) = \{\langle w'q_t'\rangle + F_P(z)\}. \tag{3}$$

The entrainment rate is w_e. Angle brackets denote a horizontal average. For the layer to remain well mixed, the energy and water fluxes $E(z)$ and $W(z)$ must be linear functions of height between $z = 0$ and the inversion height z_i:

$$E(z) = (1 - z/z_i)E(0) + (z/z_i)E(z_i), \tag{4}$$

$$W(z) = (1 - z/z_i)W(0) + (z/z_i)W(z_i). \tag{5}$$

Here, ρ_{ref} is a reference air density computed at a reference pressure of 967 mb and a time-varying reference temperature of SST $-$ 4.5 K. The net upward radiative flux F_R and the liquid water precipitation (''drizzle'') flux $F_p(z)$ (<0) are diagnosed from h_M and q_{tM} and are computed at evenly spaced grid points $z_k = k\Delta z$ following W97 and TN87, respectively. A specified cloud droplet concentration is used to compute the vertical profiles of effective radius from the cloud water profile for the radiation scheme. The precipitation flux also depends upon the cloud-top droplet mean radius as well as the cloud liquid water path.

At $z = 0$, bulk aerodynamic formulas with transfer coefficient $C_T = 0.001V(1 + 0.07V)$ (Wakefield and Schubert 1981) are used:

$$E(0) = C_TV\{h_s - h_M\} + F_R(0)/\rho_{\text{ref}},$$

$$W(0) = C_TV\{q_{ts} - q_{tM}\} + F_P(0), \tag{6}$$

where subscript s refers to saturated air at the nominal surface pressure (1022 mb) and SST. At the inversion, $\langle w'h'\rangle(z_i) = -w_e\Delta h_i$ and $\langle w'q_t'\rangle(z_i) = -w_e\Delta q_{ti}$, where $\Delta h_i = h^+(z_i) - h_M$ and $\Delta q_{ti} = q_t^+(z_i) - q_{tM}$. Hence,

$$E(z_i) = -w_e\Delta h_i + F_R^+/\rho_{\text{ref}},$$

$$W(z_i) = -w_e\Delta q_{ti}. \tag{7}$$

In the model, the radiative flux F_R^+ is the net radiative flux linearly interpolated to a height $z_i + 50$ m corresponding to a nominal top of the entrainment interface. Evaluating F_R^+ at 50 m above cloud top helps it change smoothly as z_i moves through a grid level. Using (6) and (7), we can express the fluxes $\langle w'h'\rangle(z)$ and $\langle w'q_t'\rangle(z)$ in terms of the single unknown w_e.

An entrainment closure must be used to specify w_e in terms of the knowns. The entrainment closure is usually based on a simplification of the boundary-layer-averaged turbulent kinetic energy (TKE) equation. For well-mixed subtropical convective CTBLs, in which there is little vertical shear of the mean wind except close to the sea surface and possibly the inversion, shear

generation of TKE is usually neglected. The source of TKE is upward buoyancy flux,

$$\langle w'b'\rangle(z) = (g/s_{v0})\langle w's_v'\rangle(z),$$

where the virtual static energy $s_v = C_pT_v + gz$, $T_v = T + T_{\rm ref}(\delta q_v - q_l)$ is virtual temperature (including liquid loading), $\delta = 0.608$, and s_{v0} is a reference virtual static energy. To calculate this flux, we must express s_v in terms of q_t and h. In unsaturated air ($q_l = 0$), s_v is identical to the liquid static energy s_{vl}, which is an adiabatically conserved linear combination of h and q_t:

$$s_{vl} = h - \mu L q_t,$$

where $\mu = (1 - \delta\epsilon) \approx 0.93$. In saturated air,

$$s_v = s_{vl} + [1 - (1 + \delta)\epsilon]Lq_l,$$

where $\epsilon = C_pT_{\rm ref}/L \approx 0.1$. Therefore, above cloud-base z_b, we must also express liquid water flux $\langle w'q_l'\rangle(z)$ as a linear combination of $\langle w'h'\rangle(z)$ and $\langle w'q_t'\rangle(z)$ following Lilly (1968) and Schubert et al. (1979):

$$\langle w's_v'\rangle(z) = \begin{cases} \langle w'h'\rangle - \mu L\langle w'q_t'\rangle, & 0 < z < z_b \\ \beta\langle w'h'\rangle - \epsilon L\langle w'q_t'\rangle, & z_b < z < z_i \end{cases}. \tag{8}$$

The thermodynamic coefficient $\beta \approx 0.5$ (Schubert et al. 1979; Randall 1980) is a weak function of the reference pressure and temperature.

The jump in buoyancy flux at cloud base due to the upward liquid water flux in the saturated air is a key characteristic of well-mixed CTBLs. Using the same arguments used to derive (6), we can express this jump in terms of the cloud-base fluxes of moisture and s_{vl}:

$$\begin{aligned} &\langle w's_v'\rangle(z_b^+) - \langle w's_v'\rangle(z_b^-) \\ &\quad = [1 - (1 + \delta)\epsilon]L\langle w'q_l'\rangle(z_b^+) \\ &\quad = \sigma L\langle w'q_t'\rangle(z_b) + (\beta - 1)\langle w's_{vl}'\rangle(z_b), \end{aligned} \tag{9}$$

where the thermodynamic coefficient $\sigma = \beta\mu - \epsilon \approx 0.35$. For realistic subtropical CTBLs the first term expressed in energy flux units is 20–50 W m^{-2}, while the second term tends to be much smaller, between ± 5 W m^{-2}. Thus *the cloud-base buoyancy flux jump is tightly coupled to the upward moisture flux at cloud base.*

We used the entrainment closure of TN87,

$$w_e/w^* = A/\mathrm{Ri}, \tag{10}$$

where A can be regarded as a nondimensional "entrainment efficiency." The convective velocity scale w^* is found from the vertical buoyancy flux integral

$$w^{*3} = 2.5\int_0^{z_i} dz\,\langle w'b'\rangle(z). \tag{11}$$

The bulk Richardson number $\mathrm{Ri} = gz_i\Delta s_{vi}/(s_{v0}w^{*2})$, where Δs_{vi} is the inversion jump of s_v. This entrainment closure can be written in an alternate form that will prove useful to us later,

$$w_e\Delta s_{vi} = 2.5A\overline{\langle w's_v'\rangle}, \tag{12}$$

where the overbar denotes a vertical average over the CTBL. In this alternate form, the TN87 closure is seen to be identical to a closure proposed by Deardorff (1976). Deardorff assumed that $A = 0.2$, consistent with a dry mixed layer heated from below. TN87, on the other hand, used Nicholls and Turton's (1986) linear fit to aircraft measurements in stratocumulus and a laboratory experiment of McEwan and Paltridge (1976) to specify A:

$$\begin{aligned} A &= a_1[1 + a_2(1 - \Delta s_{vm}/\Delta s_{vi})], \\ a_1 &= 0.2, \\ a_2 &= 60. \end{aligned} \tag{13}$$

Here, Δs_{vm} is twice the average of $s_v - s_{v,\rm cld}$ over all possible mixtures of air from the top of the cloud and entrained air. The factor $1 - \Delta s_{vm}/\Delta s_{vi}$ is a measure of the average evaporative cooling over all mixtures [see Nicholls and Turton (1986)]. Again, $A = 0.2$ for a dry mixed layer, but typically $A \approx$ 1–3 (tenfold more efficient entrainment) for inversion jumps and liquid water mixing ratio characteristic of subtropical stratocumulus.

At each time step, w_e is calculated using (12) as described in appendix A. Then the energy and water flux divergences can be found, and Eqs. (1)–(3) are marched forward in time using a third-order Adams–Bashforth method with a time step of 1200 s.

TABLE 1. Control run parameters.

Parameter	Value
Length of simulation	5 days
Domain height	3 km
Vertical grid spacing	25 m
SST	285 K + (1.5 K day^{-1})
Free tropospheric s^+/C_p	298 K + (3.36 K km^{-1})
Free tropospheric q_t^+	3.5 g kg^{-1}
Divergence D	3×10^{-6} s^{-1}
10-m wind V	7.1 m s^{-1}
Latitude	30 N
Water vapor path above 3 km	4 kg m^{-2}
Droplet concentration	50 cm^{-3}
Initial mixed layer s_{lM}/C_p	284.8 K
Initial mixed layer q_{tM}	7.69 g kg^{-1}
Initial mixed-layer depth z_i	413 m

b. Control run setup and results

The MLM is forced with the same idealized Lagrangian environmental conditions (Table 1) as used by W97. The SST increases at a climatologically reasonable value of 1.5 K day^{-1} following the air column, while upper-air conditions remain fixed. Diurnally averaged insolation corresponding to 23 June at a latitude of 30°N is used. The initial state of the mixed layer is the steady-state profile for the initial environmental conditions.

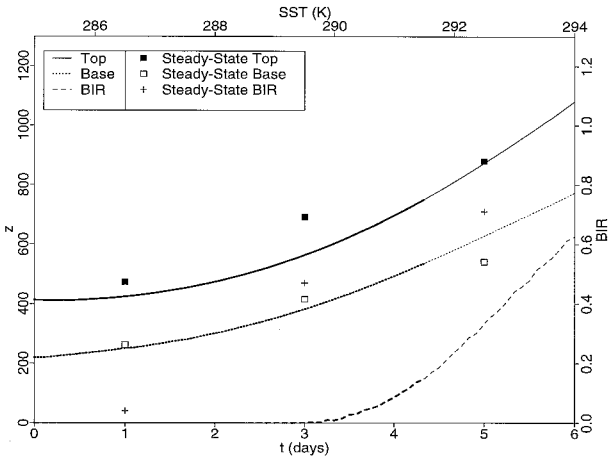

FIG. 2. Cloud base, top, and BIR (lines) during the control run. Overlaid symbols indicate steady-state runs with SSTs corresponding to 1, 3, 5 days into the control run. Lines are thickened at times when BIR < 0.15, corresponding to a coupled mixed layer.

Figure 2 shows the rising cloud base and top during the 6-day-long control run, and a predictor of decoupling for a buoyancy driven CTBL, which indicates when the mixed-layer assumption becomes inconsistent. The predictor is based on the magnitude and extent of subcloud buoyancy fluxes. Specifically, decoupling is diagnosed following Turton and Nicholls (1987) using a threshold value of the buoyancy integral ratio (BIR), also shown in Fig. 2:

$$\text{BIR} = -\int_{\substack{z < z_b \text{ at which} \\ \langle w'b' \rangle < 0}} \langle w'b' \rangle \, dz \Big/ \int_{\text{All other } z} \langle w'b' \rangle \, dz$$

$$> 0.15 \text{ for decoupling.} \qquad (14)$$

Since the purpose of the BIR is to diagnose decoupling below the turbulent convection within the cloud, only regions of negative buoyancy flux below the cloud are included in the numerator of the BIR. In two- or three-dimensional eddy-resolving numerical models, where cloud base varies between grid columns, we replace the constraint $z < z_b$ with $z < z_{b\max}$, where $z_{b\max}$ is the highest cloud base—that is, the lowest level at which all grid columns are saturated. If no such level exists, we choose $z_{b\max}$ to be the level at which the maximum fraction of grid columns are saturated.

Our predictor is not based on an exact quantitative theory of boundary layer turbulence. It represents an empirical limit on the extent to which transport of kinetic energy by boundary layer eddies allows them to penetrate regions in which they are trying to force buoyant air downward and denser air upward. We chose a threshold value of BIR (0.15) that is smaller than that chosen by Turton and Nicholls (0.4). It was chosen since published buoyancy flux measurements from aircraft (Nicholls 1984; Nicholls and Leighton 1986; Moyer and Young 1993), tethered balloon (Hignett 1991), and large eddy simulations (Moeng 1986; Krueger et al. 1995) do not document any well-mixed CTBLs in which the BIR clearly exceeds 0.15. For W97's simulations, decoupling occurs when BIR increases to 0.1–0.2 (see section 4).

From Fig. 2, we deduce that decoupling will occur at 4.3 days. The MLM is no longer physically relevant after decoupling has occurred. However, if we extend the MLM simulation out to 6 days anyway, we see that the BIR continues to rise rapidly. Hence the decoupling time is not too sensitive to the threshold; a threshold of 0.4 rather than 0.15 would delay the implied onset of decoupling only by a day.

Lastly, Fig. 2 shows the steady-state cloud base, top, and BIR for fixed environmental conditions corresponding to the SSTs at days 1, 3, and 5. This can be regarded as a limit of extremely slow rate of SST increase. The steady-state solutions have the same trends with SST as in the control run but tend to have thicker cloud, a somewhat higher inversion (except at SST = 292.5), and a substantially larger BIR. We conclude that deepening-warming decoupling occurs regardless of the rate of SST increase but occurs at a lower SST if the SST increases less rapidly following the boundary layer air column.

Figure 3 shows the warming and moistening of the control run temperature and moisture soundings. The inversion weakens as it deepens, while the air–sea temperature difference remains under 1 K throughout the simulation. The CTBL moistens only slightly as it deepens, and the air–sea mixing ratio difference increases rapidly.

Figure 4 shows profiles of the virtual static energy flux $F_{sv}(z) = \rho_{\text{ref}}\langle w's_v' \rangle$ (buoyancy flux scaled into energy flux units), the virtual liquid water static energy flux $F_{svl}(z) = \rho_{\text{ref}}\langle w's_{vl}' \rangle$ (scaled buoyancy flux in unsaturated air), and the latent heat flux $F_L(z) = \rho_{\text{ref}}L\langle w'q_t' \rangle$, multiplied by the thermodynamic coefficient σ to reflect its contribution in (9) to the jump in buoyancy flux at cloud base. The CTBL vertical average buoyancy flux is shown by the tick at the bottom of each plot. The buoyancy flux jump at cloud base increases with time. At all three times, it is comparable to the scaled moisture flux at cloud base, which more than doubles between days 1 and 5. The vertically averaged buoyancy flux varies much less. There is a compensation between positive buoyancy fluxes in the cloud layer, which increase with time, and subcloud buoyancy fluxes, which decrease with time. At three days, the subcloud buoyancy fluxes are near zero. After five days, they are markedly negative through most of the subcloud layer. The corresponding BIR of 0.3 exceeds our decoupling threshold; the mixed-layer model no longer applies. A very similar evolution of the buoyancy flux profile is seen in steady-state solutions, except that subcloud buoyancy fluxes are more negative at a given SST than in the control run, consistent with the larger BIRs in steady-state runs than in the control run.

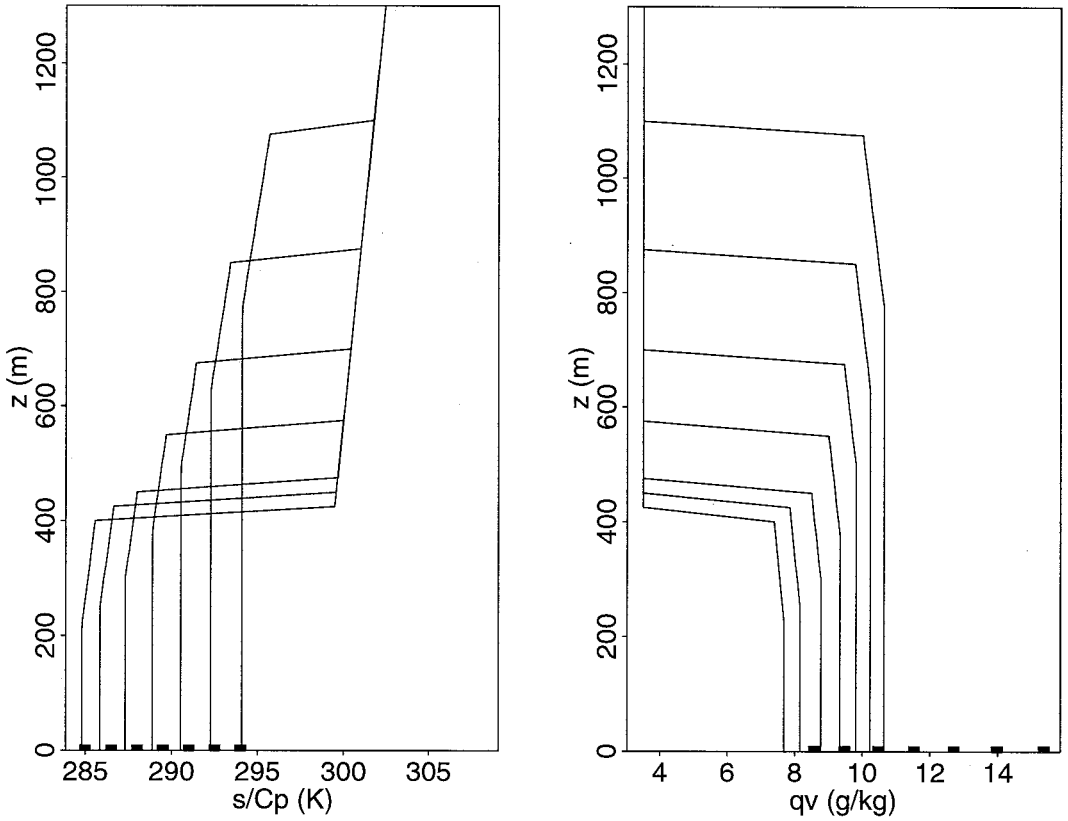

FIG. 3. Soundings of s/C_p and q_v at days 0–6 into the control run. Black rectangles at bottom indicate the SST (left) and the sea surface saturation mixing ratio (right) at these times.

Figure 5 shows time series of the surface fluxes and the diabatic forcings for the control run. The most obvious trend is a fourfold increase of the surface latent heat flux $F_L(0)$ from 35 to 140 W m^{-2}. Surface sensible heat flux remains less than 10 W m^{-2}. The net radiative flux divergence across the CTBL of combined longwave and shortwave radiation is $\Delta F_R = F_R^+ - F_R(0)$. It varies only slightly throughout the run, between 33 W m^{-2} and 42 W m^{-2}. The radiative flux divergence across the cloud layer, $\Delta F_R^{\text{cld}} = F_R^+ - F_R(z_b)$, dominates ΔF_R throughout the control run; the difference $\Delta F_R - \Delta F_R^{\text{cld}}$ indicates slight radiative warming of the subcloud layer.

The cloud-base precipitation rate is 0.5–0.9 mm day^{-1}, which produces substantial latent heating in the

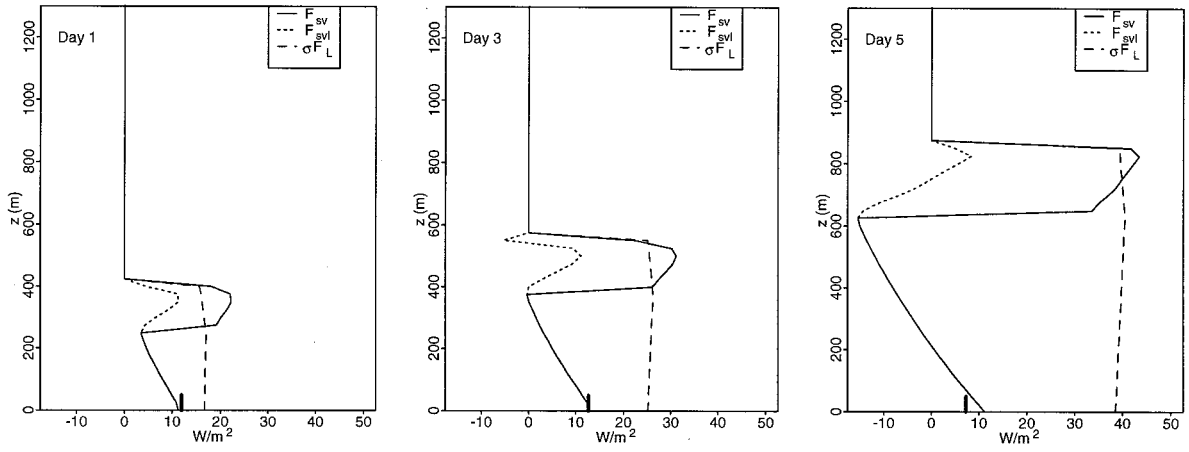

FIG. 4. Profiles of scaled buoyancy flux F_{sv}, scaled unsaturated buoyancy flux F_{svl}, and scaled latent heat flux σF_L at 1, 3, 5 days into the control run. Tick at bottom indicates CTBL vertical average of scaled buoyancy flux, $\overline{F_{sv}}$.

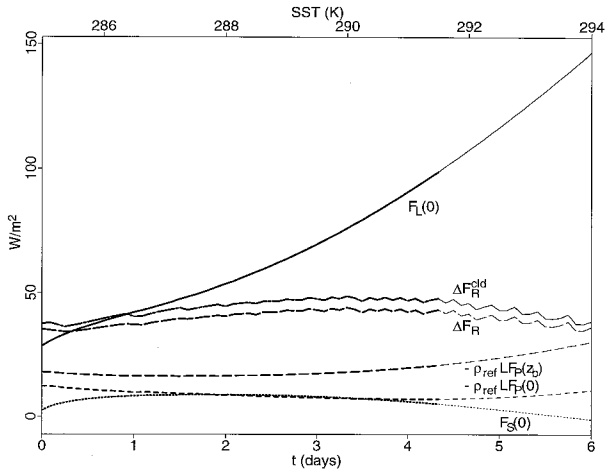

FIG. 5. Time series for the control run of surface latent heat flux $F_L(0)$ and sensible heat flux $F_S(0)$, radiative flux divergence integrated across the cloud (ΔF^{cld}_R) and across the CTBL (ΔF_R), and precipitation fluxes at the cloud base ($F_P(z_b)$) and surface ($F_P(0)$), both scaled into units of heat flux. Lines are thickened while MLM remains coupled (BIR < 0.15).

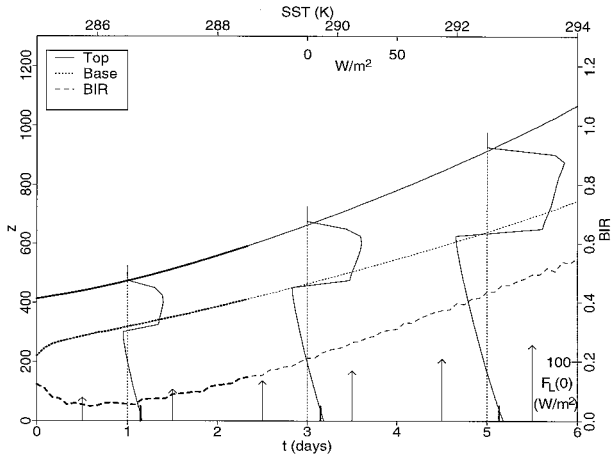

FIG. 6. Boundary layer evolution for $A = 2$ closure. Cloud base, top, and BIR as in Fig. 2. Vertical profiles of scaled buoyancy fluxes $F_{sv}(z)$ are shown at 1, 3, 5 days, referenced to the dotted vertical lines with scale at top center. Their CTBL vertical averages $\overline{F_{sv}}$ at the three times are indicated by the heavy ticks at the bottom. Vertical arrows show surface latent heat flux (scale at right).

cloud layer, $-\rho_{ref} LF_P(z_b) = 20$–$30$ W m^{-2}. Only 0.2 to 0.3 mm day^{-1} of the precipitation reaches the surface. Thus, the net latent heating of the CTBL, $-\rho_{ref} LF_P(0)$, is only 6–12 W m^{-2}.

While the CTBL remains coupled, the overall diabatic cooling due to both radiation and precipitation is 20–30 W m^{-2} in the cloud layer, 0–10 W m^{-2} in the subcloud layer, and 25–35 W m^{-2} overall. Evaporation substantially reduces the difference between the diabatic cooling in the cloud layer and that below, inhibiting convection and promoting earlier decoupling. However, since the diabatic cooling does not change greatly during the coupled phase, diabatic effects alone do not explain the timing of the decoupling.

c. *Impact of entrainment closure*

In this subsection, we describe the sensitivity of the control run to two changes in the entrainment closures. First we use a different specification of the entrainment parameter A in the TN87 entrainment closure. Then we try a totally different entrainment closure, which does not permit decoupling.

1) $A = 2$ CLOSURE

As our first sensitivity study, we used a constant $A = 2$ in the entrainment closure (10). By comparison, the evaporative enhancement of entrainment in the control entrainment closure (13) caused A to increase from 0.8 to 2.3 during the control run. The constant-A entrainment closure is also consistent with Nicholls and Turton's (1986) aircraft data, but does not match their single data point from a lab experiment (McEwan and Paltridge 1976) in which radiative but not evaporative cooling was active. Since the experiment used a different working fluid and much lower Reynolds number, one might argue that the laboratory data point is not commensurate with the aircraft measurements.

Figure 6 shows the CTBL evolution with the $A = 2$ closure. The cloud base and cloud top evolve remarkably similarly to the control run. The BIR is larger than in the control run for the shallow CTBL, and the BIR $= 0.2$ decoupling threshold is reached a day earlier, but the BIR again increases as the CTBL deepens. The same decoupling mechanism is evident as in the control run. The surface latent heat flux is similar to the control run, rapidly increasing as SST rises. The buoyancy flux jump across cloud base increases proportional to the latent heat flux, while the CTBL-averaged buoyancy flux remains nearly constant. Correspondingly, the cloud-layer buoyancy fluxes increase but the subcloud fluxes decrease, inducing decoupling.

2) SCHUBERT $\kappa = 0.5$ CLOSURE

The control and $A = 2$ entrainment closures can both be classified as w^* closures, in which vertically integrated buoyancy fluxes are an energy source for large mixed-layer-filling eddies with the convective velocity scale w^*. These eddies are assumed to entrain at a rate independent of the vertical distribution of buoyancy fluxes. The original (and still widely used) entrainment closures used in studies of cloud-topped mixed layers have been ''flux partitioning'' closures. Such closures (e.g., Lilly 1968; Kraus and Schaller 1978; Schubert et al. 1979) assume that the entrainment rate adjusts so that some measure of the negative buoyancy fluxes within the subcloud layer is a fixed fraction of the kinetic energy generation by positive buoyancy fluxes else-

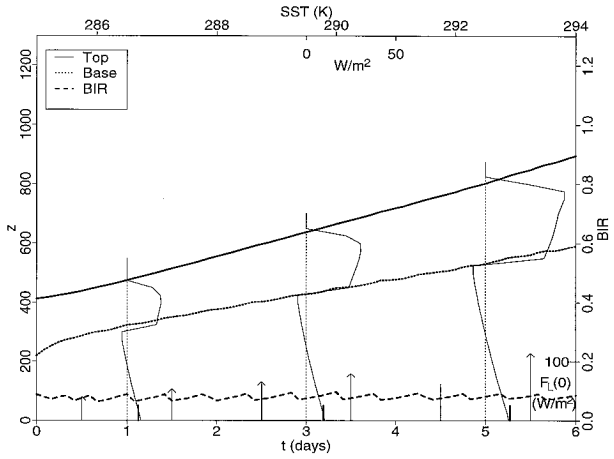

Fig. 7. As in Fig. 6 but with the Schubert flux-partitioning entrainment closure.

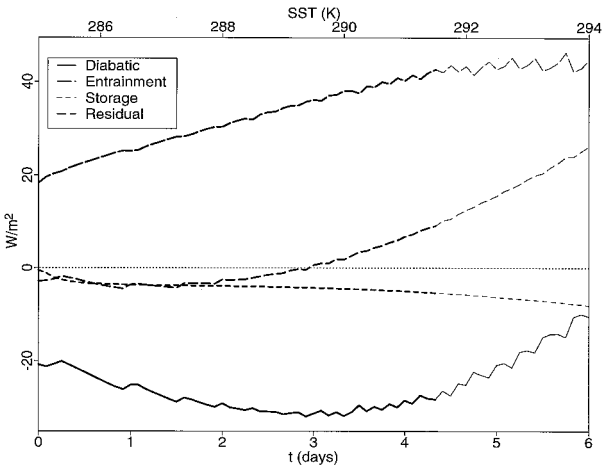

FIG. 8. Terms in the cloud-layer energy balance of the control run. Lines are thickened while MLM remains coupled (BIR < 0.15). Zero indicated by dotted reference axis.

where in the CTBL. By construction, these closures maintain a constant or nearly constant BIR and do not allow boundary layer decoupling by the mechanism we and TN87 rely upon.

The impact of using such a closure in the control run is seen in our second sensitivity study, in which we use the Schubert et al. (1979) closure

$$\langle w'b'\rangle(z_b^-) = -k\int_0^{z_i} dz\,\langle w'b'\rangle(z), \qquad k = 0.5. \quad (15)$$

In Fig. 7 we see that cloud base, top, and latent heat flux evolve rather similarly to the $A = 2$ closure and the control run, and the buoyancy flux shows a similarly increasing jump at cloud base. However, the subcloud buoyancy fluxes remain only slightly negative and the BIR remains slightly under 0.1 throughout. In contrast to the TN87 closures, we see in Fig. 7 that the vertically averaged buoyancy flux increases steadily during the run. This subtle change allows the buoyancy jump at cloud base to increase while the subcloud buoyancy flux remains near zero and the CTBL remains coupled.

We draw two major conclusions from this comparison of entrainment closures. First, *the impact of the closure on the bulk CTBL evolution is surprisingly small, as long as the CTBL remains well mixed.* This is a reason that nearly 30 years of study have not adequately resolved which entrainment closure is correct. Instead, *the key role of the entrainment closure is to diagnose when the mixed-layer assumption will fail and decoupling occurs.*

Both types of closure are consistent with observations of dry boundary layers heated from below. However, observations of shallow nocturnal stratocumulus (e.g., Moyer and Young 1993, case 3) and Moeng's (1986) large-eddy simulation show that buoyancy fluxes can be positive throughout the subcloud layer. This is not consistent with the flux-partitioning closures cited above. Flux-partitioning closures also cannot explain the observations and numerical simulations mentioned in the introduction, which indicate that decoupling generally does occur as the CTBL warms and deepens.

3. Cloud-layer energy balance

The insensitivity of mixed-layer evolution to the entrainment closure occurs because ''energy balance'' of s_{vl} in the cloud layer largely determines the entrainment rate into subtropical CTBLs. The energy budget of the cloud layer can be obtained from integration of (2) and (3) over the cloud layer:

$$\underbrace{\rho_{\text{ref}} w_e (s_{vl}^+(z_i) - s_{vlM})}_{\text{(Entrainment)}} - \underbrace{\Delta F^{\text{cld}}_{R+P}}_{\text{(Diabatic)}} + \underbrace{\delta z_c \rho_{\text{ref}} ds_{vlM}/dt}_{\text{(Storage)}} = \underbrace{R = -\rho_{\text{ref}}\langle w' s_{vl}'\rangle(z_b)}_{\text{(Residual)}} \approx 0. \quad (16)$$

Here, δz_c is the cloud-layer thickness, and the in-cloud diabatic flux divergence $\Delta F^{cld}_{R+P} = \Delta F_R^{\text{cld}} + \mu L F_p(z_b)$. The residual flux R is the downward s_{vl} flux through the cloud base, which is proportional to the downward buoyancy flux just below cloud base. Figure 8 shows the budget terms for the control run. During the coupled phase, the budget is dominated by entrainment warming and diabatic cooling. Throughout the coupled phase, the residual flux is much smaller than the entrainment and diabatic terms. The storage term is also small. The other entrainment closures discussed above have similar budgets.

Thus, a good approximation to the entrainment rate for almost any entrainment closure can be obtained by neglecting the subcloud buoyancy flux in (16) and solving for the energy balance entrainment rate w_e^E. This was called the ''minimum entrainment'' closure by Lilly (1968) and is also equivalent to the Schubert entrainment closure with $k = 0$:

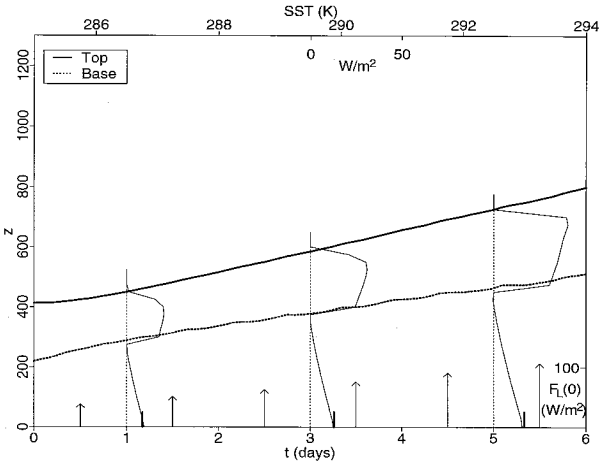

FIG. 9. As in Fig. 6 but for the energy balance entrainment closure.

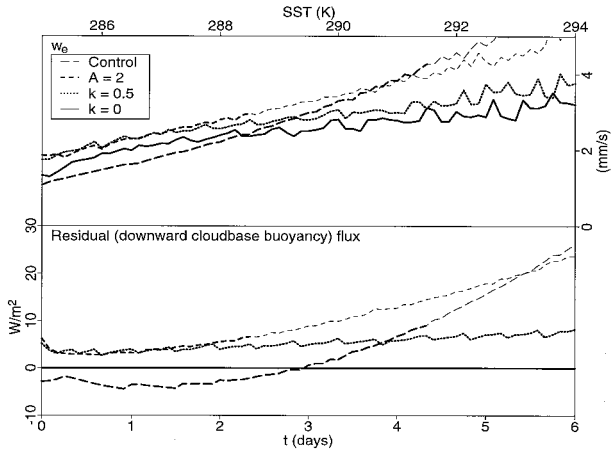

FIG. 10. Entrainment rate (top) and residual flux (bottom) for the four entrainment closures: Control (TN87 with variable A), TN87 with fixed $A = 2$, Schubert flux-partitioning closure with $k = 0.5$, and energy balance closure ($k = 0$ curve). Lines are thickened while MLM remains coupled (BIR < 0.15).

$$w_e^E = -(\Delta F_{R+P}^{\text{cld}}\rho_{\text{ref}} + \delta z_c ds_{vlM}/dt)/(s_l^+(z_i) - s_{vlM}). \quad (17)$$

While the storage term is also small, there is no real advantage to neglecting it.

We tried the energy balance entrainment closure in place of the TN87 closure in the control run. As expected, the evolution of cloud base, top, and latent heat flux plotted in Fig. 9 are very similar to the earlier closures. The buoyancy flux profiles are quite similar to the Schubert closure shown in Fig. 7. Since subcloud buoyancy flux is zero by construction, there is no region of negative buoyancy flux and BIR $= 0$.

The top graph of Fig. 10 compares the entrainment rates for the other entrainment closures to the energy balance prediction. The bottom graph shows the residual, or downward buoyancy flux, for the entrainment closures. More entrainment of buoyant above-inversion air produces more negative subcloud buoyancy fluxes, since the high s_{vl} air must be mixed down through the entire CTBL. Hence, to produce a downward subcloud buoyancy flux requires slightly more entrainment than predicted by the energy balance closure. Similarly, an upward buoyancy flux below cloud base (negative residual flux) indicates slightly less entrainment than predicted by the energy balance closure. Figure 10 shows that the control run (long-dashed line) starts with upward subcloud buoyancy fluxes (negative residual flux), and a lower entrainment rate than the energy balance closure (solid line), and switches after three days to downward subcloud buoyancy fluxes and a lower entrainment rate than the energy balance closure. The discrepancy in w_e becomes increasingly large as the control run becomes decoupled and the residual flux becomes sizeable. The $k = 0.5$ Schubert and the $A = 2$ closures both maintain a region of downward buoyancy fluxes throughout the simulation, and have entrainment rates slightly larger than the energy balance prediction.

Nevertheless, the main point to be drawn from Fig. 10 is that while the CTBL remains coupled, the residual flux remains small and the energy balance entrainment estimate is accurate to within 25% or better for all of the entrainment closures tested, regardless of type. This result may appear paradoxical—how can quite different entrainment closures give such similar results? Our answer is as follows: both w^* and flux-partitioning closures typically determine entrainment rate using the buoyancy flux profile. A small increase in entrainment rate produces a sizeable decrease in the buoyancy fluxes, especially below cloud base. Hence, small deviations of the entrainment rate from w_e^E can create a sufficient range of buoyancy flux profiles to satisfy most entrainment closures.

4. A minimal model of the decoupling transition

To understand more clearly how decoupling is connected to the environmental parameters and the entrainment closure, we focus on a ''minimal'' MLM of a radiatively driven CTBL simple enough to be analyzed further. We assume the following:

1) a steady state (SST independent of time).
2) no drizzle.
3) a fixed radiative flux divergence ΔF_R concentrated at the cloud top. Because this is the only diabatic forcing in the CTBL, its effect on the overall heat budget could be compared to the sum of the CTBL radiative flux divergence and latent heating in the control run, which was 25–35 W m^{-2}. However, convection is what induces entrainment and promotes decoupling. Concentrated cloud-top cooling is much more efficient than the actual diabatic heating profile in forcing vigorous convection. To estimate a ΔF_R that produces a similar intensity of convection as in the control run, we subtracted the mean subcloud diabatic cooling rate from the cloud-layer cooling

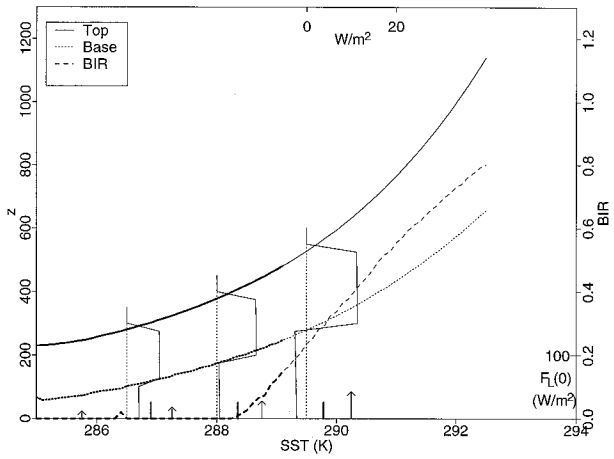

FIG. 11. As in Fig. 6 but for the steady-state minimal model with constant cloud-top cooling $\Delta F_R = 15$ W m^{-2}. SSTs correspond to the times in Fig. 6.

rate over the coupled period of the control run. We then integrated over the boundary layer depth to obtain $\Delta F_R \approx 15$ W m^{-2}.

4) here, Δs_{vli} used in place of Δs_{vi} in the TN87 entrainment closure. The difference $\Delta s_{vli} - \Delta s_{vi} = (1 - (1 + \delta)\epsilon)Lq_{li}$, where q_{li} is the cloud-top liquid water mixing ratio, is typically no larger than 1 kJ kg^{-1}, compared to a typical Δs_{vi} of 10 kJ kg^{-1}.

Except for the entrainment closure, this model is the same as was analyzed by Lilly (1968). Figure 11 shows the cloud base, cloud depth, and BIR derived from the minimal MLM with $\Delta F_R = 15$ W m^{-2} and the environmental conditions of the control run. To span the range of SSTs in the control run while maintaining a good approximation to steady-state conditions, we increase SST very slowly at 0.075 K day^{-1} over a 100 day run.

Figure 11 also shows the buoyancy flux profiles and the surface latent heat flux at selected times. As in the control run, latent heat flux increases rapidly with SST. The cloud-base jump in buoyancy flux increases proportional to latent heat flux, while the CTBL-average buoyancy flux decreases, but much more slowly. In-cloud buoyancy flux goes up, while subcloud buoyancy flux decreases with increasing SST. Overall, the minimal MLM shows qualitatively the same behavior as the control and $A = 2$ runs, despite the simplified diabatic heating profile.

a. Flux-ratio minimal decoupling condition

For the minimal MLM, it is straightforward to determine when negative subcloud buoyancy fluxes are required to sustain a mixed layer. The resulting criterion, which we now derive, is remarkably simple and enlightening. It can be regarded as a reinterpretation of Lilly's minimum entrainment closure (the energy balance entrainment closure of zero buoyancy flux at cloud base) as a ''minimum decoupling condition.'' Decoupling requires sufficient negative buoyancy fluxes to produce BIR > 0.15, which requires a somewhat stricter and much less elegant criterion with a similar physical interpretation.

For a steady-state cloud-topped mixed layer in the absence of internal sources [i.e., with no radiative flux divergence except at the cloud top and no drizzle flux, as implied by assumptions (i)–(iii)], the fluxes of h and r are constant with height. If in addition the subcloud buoyancy flux is zero, (8) reduces to

$$\langle w's_v'\rangle(z) = \begin{cases} 0, & 0 < z < z_b \\ \sigma L\langle w'q_t'\rangle(0), & z_b < z < z_i \end{cases}. \quad (18)$$

The entrainment rate can then be found from (10),

$$w_e = Aw^{*3}/(z_i g \Delta s_{vli}/s_{v0}). \quad (19)$$

Rearranging (19), and determining w^* from the buoyancy flux profile (18), we deduce that

$$w_e \Delta s_{vli} = A\eta(\delta z_c/z_i)L\langle w'q_t'\rangle(0), \quad (20)$$

where $\eta = 2.5\sigma \approx 0.9$ is a weak function of pressure and temperature.

On the other hand, the energy balance (16) for s_{vl} in the steady-state cloud layer of the minimal model is

$$w_e \Delta s_{vli} - \Delta F_R/\rho_{\text{ref}} = R = -\langle w's_v'\rangle(z_b^-).$$

The energy balance entrainment rate w_e^E is obtained by neglecting R. Therefore,

$$w_e > w_e^E = \Delta F_R/(\rho_{\text{ref}}\Delta s_{vli}) \text{ for } \langle w's_v'\rangle(z_b^-) < 0. \quad (21)$$

Substituting (20) into (21), we can deduce the criterion for negative subcloud buoyancy fluxes in the minimal model:

$$\Delta F_R/F_L(0) < Q \equiv A\eta(\delta z_c/z_i) \text{ for } \langle w's_v'\rangle(z_b^-) < 0. \quad (22)$$

This ''minimal decoupling'' criterion can be regarded as the broadest possible criterion for decoupling—that *any* negative buoyancy fluxes below cloud base indicate decoupling.

According to (22), three critical parameters govern deepening-warming decoupling in the minimal model. Decoupling occurs when the ''flux-ratio'' $\Delta F_R/F_L(0)$ of the CTBL radiative flux divergence to the surface latent heat flux becomes sufficiently small. The threshold ratio Q is proportional to the fraction of the CTBL depth filled with cloud, $\delta z_c/z_i$, and the entrainment efficiency A. Using typical values for a subtropical CTBL, if the cloud fills 25% of the depth of the CTBL and $A = 2$, negative subcloud buoyancy fluxes occur if the threshold ratio $\Delta F_R/F_L(0) < 0.45$, or $F_L(0) > 90$ W m^{-2} for a ΔF_R of 40 W m^{-2}. Decoupling occurs more readily if a large fraction of the CTBL is filled by cloud, or if the entrainment efficiency A is large.

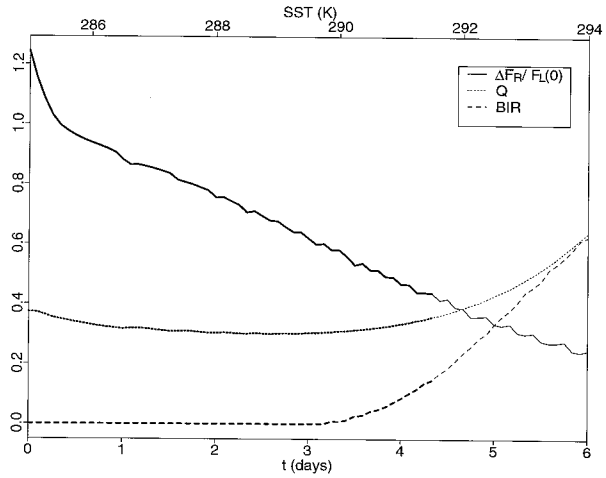

FIG. 12. Time series of $\Delta F_R/F_L(0)$, its ideal threshold value $Q = A\eta(\delta z_c/z_i)$ and BIR for the control run. Lines are thickened while MLM remains coupled (BIR < 0.15).

b. Flux ratio condition for full MLM physics

How well does (22) hold when we relax the ''minimal'' assumptions of a steady-state, no drizzle, and radiative flux divergence concentrated at cloud top? We can test this in the control run. In Fig. 12, we see that negative buoyancy fluxes (nonzero BIR) first occur at approximately 3 days, while the flux ratio $\Delta F_R/F_L(0)$ drops to its threshold value Q at 4.5 days, when BIR ≈ 0.2. The subcloud buoyancy fluxes are more negative than predicted by the ''minimal'' model due mainly to drizzle, as discussed below. During the control run ΔF_R remains nearly constant while latent heat flux increases fivefold, from 29 to 148 W m^{-2}, so the flux ratio decreases fivefold over the run. The threshold Q varies much less. We conclude it is primarily the increase in latent heat fluxes that is driving the deepening-warming decoupling. For the TN87 entrainment closure, a rule of thumb is that a typical subtropical CTBL will decouple when surface latent heat fluxes rise to 100 W m^{-2} or more.

In appendix B, the minimal decoupling criterion is generalized to include all effects not in the minimal MLM, resulting in a criterion identical to (22) except that the cloud-top radiative flux divergence ΔF_R is replaced by a more comprehensive diabatic forcing ΔF_{diab}:

$$\Delta F_{\text{diab}}/F_L(0) < Q \quad \text{for} \quad \langle w'b'\rangle(z_b^-) < 0,$$

$$\Delta F_{\text{diab}} = \Delta F_R - S, \tag{23}$$

$$S = k_v ds_{vlM}/dt + k_q dq_{tM}/dt + S_R + S_P + S_C. \tag{24}$$

Here, k_v and k_q are functions of z_b/z_i and S_R, S_P, and S_C are terms due, respectively, to the vertical distribution of radiational heating within the CTBL, to precipitation and evaporation, and to the liquid water in the cloud. These terms are given in appendix B, (B6)–(B10). They involve weighted vertical integrals over the entire CTBL and do not have simple physical interpretations in terms of cloud layer or CTBL-integrated diabatic flux divergences. Positive terms in the correction term S reduce ΔF_{diab} and promote decoupling.

The terms that S comprises vary little with time in the control run. Three days into the control run, the subcloud buoyancy flux crosses zero. At this time, $S = 23$ W m^{-2}, which is a sizeable fraction of the $\Delta F_R = 42$ W m^{-2} and reduces the diabatic forcing ΔF_{diab} to 19 W m^{-2}. The dominant term is precipitation-induced decoupling, $S_P = 26$ W m^{-2}. Precipitation and subcloud evaporation is reducing ΔF_{diab} and promoting decoupling as effectively as a nearly threefold increase in latent heat fluxes! While they are not necessary to induce decoupling, cloud microphysical effects strongly affect how easily it occurs through their effect on precipitation rates. The precipitation rates in the control run are quite reasonable. Many subtropical CTBLs are observed to contain no measurable drizzle, but sustained surface precipitation rates in shallow subtropical CTBLs of up to 1 mm day^{-1} for 24 h, substantially stronger than in the control run, have been observed in pristine marine air masses (Bretherton et al. 1995).

The other terms in S are much smaller. The radiation offset $S_R = -6$ W m^{-2} is due to the heating being distributed in the CTBL rather than all being at cloud top. The cloud-top longwave cooling contributes negligibly to this offset since it is concentrated near cloud top. The shortwave absorption and longwave cloud base heating both stimulate more buoyancy fluxes than if they were moved up to the layer top, so the radiation offset acts against decoupling. The cloud liquid water offset $S_C = 3$ W m^{-2} and the offsets due to CTBL warming and moistening are $k_v ds_{vl}/dt = 3$ W m^{-2} and $k_q dq_{tM}/dt = -3$ W m^{-2}.

Note that (23) is also applicable to diurnal decoupling, where the dominant balance of terms is very different. For instance, for shallow coastal stratocumulus the net boundary layer radiative flux divergence ΔF_R can be 60 W m^{-2} at night and zero during the day, when in-cloud solar absorption approximately cancels cloud-top longwave cooling (Nicholls 1984). This is much larger than the typical diurnal variations in the latent heat flux or any of the other terms in (22). As expected, the diurnal variation of ΔF_R promotes decoupling during the day according to (22).

c. Conceptual view of subtropical mixed-layer evolution and deepening–warming decoupling

The feedbacks decribed below that lead to deepening-warming decoupling in our model are diagrammed in Fig. 13. With the TN87 entrainment closure, we have found that decoupling occurs because, as the sea surface warms.

1) The cloud base jump in buoyancy flux, which is

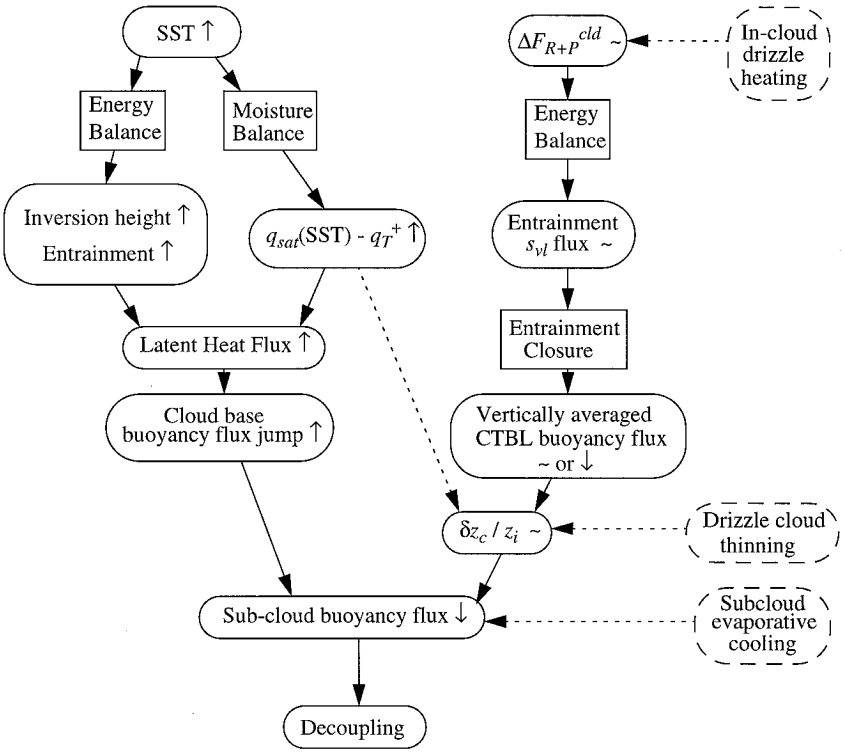

FIG. 13. Mechanism of deepening-warming decoupling. Rounded rectangles indicate time-varying fields. Here, ↑, ~, ↓ indicate whether a field increases, stays fairly constant, or decreases as SST rises. Dashed rectangles indicate important effects of drizzle on decoupling. True rectangles indicate processes or closure assumptions. Arrows indicate feedbacks central to deepening-warming decoupling. Dotted arrows indicate feedbacks that impact but are not required for deepening-warming decoupling. See text for further discussion.

proportional to surface latent heat flux, increases (Fig. 13, left of center).

2) The CTBL vertical average buoyancy flux does not increase (Fig. 13, right of center).

Thus, the cloud-layer buoyancy flux increases but the subcloud buoyancy flux decreases, leading to decoupling. In this subsection, we aim to understand why 1) and 2) hold.

Point 1) depends on the energy and moisture balance of the boundary layer, and is largely independent of the entrainment closure. The top-left section of Fig. 13 shows the key processes. As SST rises, the boundary layer warms almost in lockstep. Suppose, in accordance with our simulations, that the total cloud-layer diabatic forcing, due mainly to radiative flux divergence, does not change too much as SST changes. This is a reasonable assumption as long as the CTBL remains cloud covered. Also suppose for simplicity in this discussion that horizontal divergence and above-inversion thermodynamic profiles remain fairly constant; this is not central to our argument. Maintenance of energy balance requires that as SST rises, the inversion rises and weakens in strength, and that entrainment rate rises. In the moisture balance of the CTBL, the larger entrainment rate and the larger difference between the saturated sea surface mixing ratio and the above-inversion mixing ratio both contribute to an increasing difference between the mixed-layer mixing ratio and the sea surface mixing ratio with rising SST. This implies a known and rising cloud base, and a rapid rise in latent heat fluxes with SST.

Unlike point 1), point 2) does depend on the entrainment closure. It is diagrammed in the center-right portion of Fig. 13. Energy balance requires an approximate balance between entrainment warming and cloud layer diabatic cooling of the form (21). Turbulent kinetic energy generation by buoyancy fluxes adjusts to maintain the required entrainment rate. For a TN87-type entrainment closure (12) this ties the vertically averaged buoyancy flux to the cloud-layer diabatic cooling $\Delta F_{R+P}^{\rm cld}$ [note this is similar to, but not the same as the diabatic forcing $\Delta F_{\rm diab}$ of(23)],

$$2.5A\overline{\langle w's_v'\rangle} \approx \Delta F_{R+P}^{\rm cld}/\rho_{\rm ref}. \qquad (25)$$

The diabatic cooling remains comparatively constant (Fig. 5), while the entrainment efficiency A tends to increase with SST if it is allowed to vary according to (13). Thus (as seen in Figs. 4 and 11), the vertically averaged buoyancy flux tends to slowly decrease with increasing SST.

We have emphasized the role of increasing latent heat fluxes in generating deepening-warming decoupling by decreasing the flux ratio. Time variations in other parameters in (23) also affect when the decoupling occurs, but are not as fundamental. The threshold ratio Q is proportional to the fraction of the layer filled by cloud, $\delta z_c/z_i$, and the entrainment parameter A. With the minimal model, we saw that for a nonprecipitating CTBL, $\delta z_c/z_i$ is a rather weaker function of SST than is the flux ratio. The variation of A with SST in the control run is large, but we found that decoupling occurs even if A is constant. Thus, time variation in Q does not appear to be vital to decoupling.

The most important effects of precipitation on decoupling are indicated on the far right of Fig. 13. Precipitation is best viewed as an important modifier of deepening-warming decoupling rather than its fundamental cause, so we have indicated the effects with dotted arrows. Precipitation promotes CTBL decoupling by decreasing the diabatic forcing ΔF_{diab}. This forcing comes both from in-cloud latent heating due to drizzle falling through cloud base and from subcloud evaporation. The in-cloud latent heating reduces the diabatic cooling in the cloud layer. Working down the influence chain, this promotes decoupling by decreasing the entrainment s_{vl} flux and hence the vertically averaged buoyancy flux. The subcloud evaporation promotes decoupling, too, by creating a local minimum in buoyancy fluxes at the top of the cooling region, that is, just below cloud base. However, precipitation also indirectly works against decoupling by inhibiting thickening of the cloud layer, reducing $\delta z_c/z_i$.

5. Comparison of MLM with two-dimensional eddy-resolving simulations

W97, using a two-dimensional eddy-resolving model (ERM) with the same environmental conditions, find a deepening and decoupling of the CTBL qualitatively similar to the control run. The mean cloud thickness of 150–200 m during the first four days is similar to the control run. However, the inversion deepens more rapidly in their simulations, rising from 600 m (the steady state in the eddy-resolving model for the initial environmental conditions) to 980 m after three days and 1480 m after six days (Fig. 14a).

In W97's simulation, decoupling starts after 2.5 days, substantially sooner than seen in the control run. This can be seen in Fig. 14a by comparing the lowest cloud base in any grid column of the model with the mean cloud base. All air in a well-mixed CTBL has a similar LCL, while in a decoupled boundary layer, cumulus updrafts rising from the surface layer are moister and have a substantially lower cloud base than the overlying stratocumulus. In W97's simulation, cumulus convection is intermittent in time due to the small domain size, so after decoupling the hourly average lowest cloud base lies between the typical cumulus cloud base and the stratocumulus cloud base and therefore overestimates the cumulus cloud base. During the first 2.5 days, the lowest cloud base in the model domain is only 100 m below the mean cloud base, indicating a relatively well-mixed distribution of LCLs. After 2.5 days, the height difference between the lowest cloud base and the mean cloud base starts to increase.

Before day 2.5, the BIR (Fig. 14a) rises from near zero to 0.1. As decoupling begins during days 2.5–3, the BIR rises to 0.15. Later in the simulation, the BIR continues to oscillate around 0.15 due to a zone of negative buoyancy fluxes around the cumulus cloud base. Hence, the circulation pattern changes during decoupling to prevent further rise of the BIR.

We might expect better agreement between the MLM and the ERM. In the rest of this section, we show that with appropriate modifications the MLM can reproduce W97's results well up until the time of decoupling, and that the decoupling criterion derived in the previous section is consistent with the ERM. It is illuminating to examine several reasons that modifications are needed.

The analysis of the previous sections suggests that the timing of decoupling is sensitive to the entrainment closure, that is, the details of the entrainment process. Since this is represented so differently in the two models we might anticipate disagreement about this timing. In fact, the A diagnosed by W97 for the first four days of their run is 3.5–5, rather larger than the $A = 0.6$–2.5 during the control MLM run. According to (23), this should promote earlier decoupling in the ERM than the MLM run, as we have found.

However, we also showed that the inversion height is insensitive to the entrainment closure. Why, then, does the W97 simulation show a much more rapid inversion rise? In fact, we can identify two other salient differences between W97's simulation and the control run.

1) W97's procedure for relaxing the sounding to the prescribed structure was applied only at least 150 m above the inversion height to minimize interference with the entrainment process. Due to strong radiative cooling in the lowest 150 m above the inversion, the temperature just above the inversion averaged 2.5 K cooler than the prescribed value used in the MLM during days 0–4.
2) Drizzle rates in W97's simulation averaged 0.2 mm day^{-1} at cloud base and near zero at the surface, significantly lower than the 0.5–1 mm day^{-1} at cloud base and 0.2–0.3 mm day^{-1} at the surface in the control run. Thus, the radiative cooling in the control run was counterbalanced by 5–7 W m^{-2} of net latent heating that was not present in W97's simulation, enhancing entrainment rates. Despite the lower drizzle rate, mean cloud thickness was lower in W97 than in the control run.

We examine the impact of these differences by making three modifications to the MLM. First, we lower the

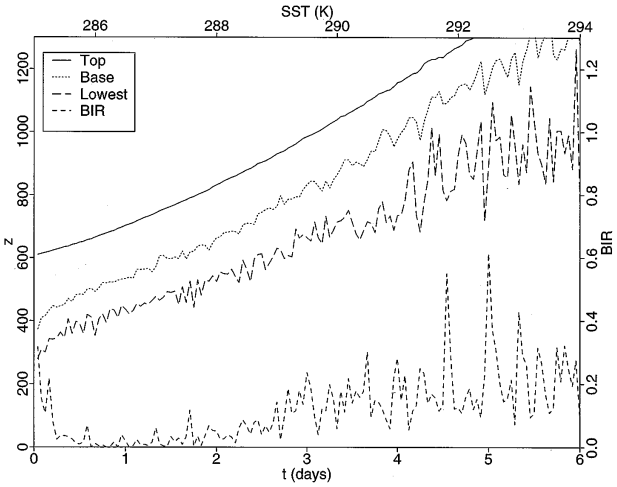

FIG. 14. (a) As in Fig. 2 but for hourly averages from W96's eddy-resolving model. ''Base'' refers to mean cloud base, while ''lowest'' refers to lowest cloud base.

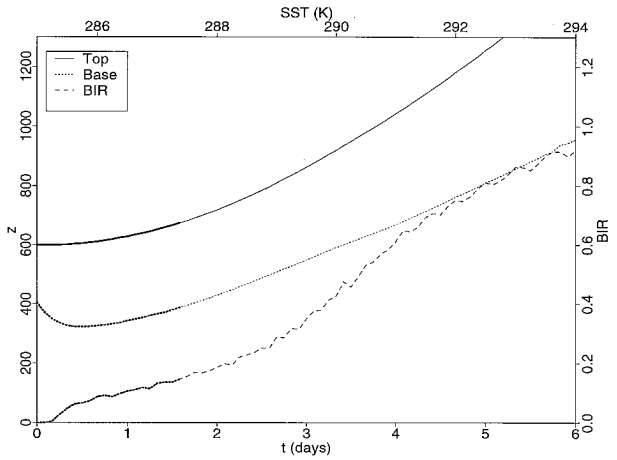

FIG. 14. (b) As in Fig. 2 but for MLM with modified drizzle parameterization and s^+/C_p modified to better match W96's eddy-resolving model.

above-inversion s^+/C_p by 2.5 K to mimic 1). Second, we double the threshold droplet size r_v* for efficient autoconversion in the TN87 drizzle parameterization from 10 μm to 20 μm to mimic 2). Third, we initialize the MLM with a deeper $z_i = 600$ m and initial cloud thickness of 200 m similar to W97's initial conditions. The combined impact of these modifications to the MLM control run (Fig. 14b) is to cause the inversion to deepen faster (to 866/1496 m after three/six days in the modified run, compared to 563/1081 m after three/six days in the control run), while cloud thickness remains close to 250 m during the first three days, slightly thicker than in W97. Cloud base drizzle fluxes are reduced to 0.2 mm day^{-1}, approximately to those found by W97.

Most of the extra deepening in the modified run is due to the lower s^+/C_p. When the MLM is modified by changing s^+/C_p and the initial conditions but not the drizzle parameterization, the three/six day inversion heights are 765/1365 m. When the MLM is modified by changing the drizzle parameterization and the initial conditions, but not s^+/C_p, the three/six day inversion heights are 687/1208 m. In the latter case, the reduced latent heating due to drizzle suppression is partly canceled by increased solar absorption due to a slightly thicker cloud layer. Hence, the net CTBL diabatic cooling available to balance entrainment warming is only slightly increased from the control run and little extra deepening occurs.

The MLM BIR is between 0.1 and 0.2 through most of the first two days, quite comparable to W97. It then rises slowly to 0.35 after three days (suggesting decoupling should take place after two days, a little earlier than found by W97) and more rapidly thereafter.

The MLM A varies from 1.0 initially to 2.0 at three days, rising to 7.1 at six days. During the first three days, this A is smaller than in W97's simulation, even though the BIR is comparable. We can mimic W97's diagnosed A more closely by using the entrainment closure $A = 4$ in the modified control run. As expected from the energy balance arguments, this makes only a minor change in inversion height (to 939/1479 m after three/six days) and has little impact on the cloud thickness during days 1–3. However, during days 1–3, the BIR with the $A = 4$ closure was 0.4–0.65, much larger than the BIRs of 0.1–0.2 found in W97. Two possible reasons why use of the larger A in the MLM does not improve its agreement with the ERM are as follows. First, in the ERM, there is a slight decrease of mixing ratio with height (0.5 g kg^{-1} over the CTBL depth) even in the ''well-mixed'' CTBL. This decreases cloud thickness by up to 50% compared to a perfectly well-mixed layer, for a given entrainment rate and surface fluxes. Thus, w* for the MLM will be larger than for the ERM and a lower ''effective A'' (by up to 50%) in the MLM is necessary to sustain the same entrainment rate and BIR as in the ERM with the same surface fluxes. Second, entrainment in the ERM and in reality takes place in a zone that is 25–50 m or so thick. In this region, where unsaturated air is pulled down into the cloud, the buoyancy fluxes can be negative even though the MLM (which assumes instantaneous mixing and evaporative cooling associated with entrainment through the inversion) predicts positive buoyancy fluxes right up to the inversion. This again leads to higher estimates of w* for a given cloud thickness, surface fluxes, and entrainment rate in an MLM than in an ERM. To get the same BIR as in the ERM, we must again use a lower ''effective A'' in the MLM.

The flux-ratio decoupling criterion (22) based on the ratio of radiative cooling to moisture flux works just as well for the eddy-resolving model results as for the MLM. Between days 0 and 4, W97 found that the latent heat flux $F_L(0)$ tripled from 25 to 70 W m^{-2}, while the net CTBL radiative flux divergence $\Delta F_R \approx 35$ W m^{-2}, the fractional cloud thickness $\delta z_c/z_i \approx 0.3$, the entrainment parameter $A \approx 4$, and hence the threshold parameter $Q = A\eta(\delta z_c/z_i)$

$\approx$ 1.1 throughout. According to (22), decoupling should occur in the ERM when $F_L(0)$ exceeds $\Delta F_R/Q \approx 32$ W m^{-2}. In fact, at the onset of decoupling after 2.5 days, W97's latent heat flux is 55 W m^{-2}. If we lower A to the "effective" $A \approx 2$ that produced good agreement between MLM and ERM BIRs, Q is only half as large and the latent heat flux corresponding to the onset of decoupling is $\Delta F_R/Q = 64$ W m^{-2}, in better agreement with (22). Note that we have not considered the drizzle correction (24) to the diabatic cooling, since it is much smaller in this comparison than in the control run.

We conclude from this comparison that the decoupling process seen in eddy-resolving models of the stratocumulus to trade cumulus transition can be understood as in the MLM. Furthermore, the boundary layer evolution in a diurnally averaged eddy-resolving model is very similar to an MLM under the same environmental conditions, as long as the effect of the strong longwave cooling in the lowest few hundred meters above the inversion is accounted for. This can be done either by adding an appropriate cold offset to the above cloud sounding in the MLM (as done here) or by adding this above-inversion cooling into the radiative flux divergence at cloud top in the MLM.

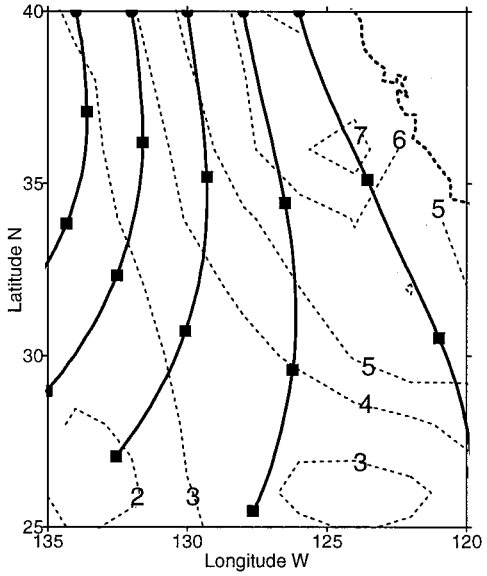

FIG. 15. (a) July climatological trajectories (solid) used in northeast Pacific MLM integrations and horizontal divergence (dash, units of 10^{-6} s^{-1}). Heavy dashes indicate coastline. Half-octagons indicate starting location of air columns, and squares indicate air-column positions at 1, 2, and 3 days.

6. The regional extent of decoupling in subtropical CTBLs

In this section, we examine the relevance of deepening–warming decoupling to the northeast Pacific subtropical stratocumulus regime. We use the method of Wakefield and Schubert (1981) of following MLM-predicted boundary layer evolution along climatological trajectories of boundary layer air columns. We use July climatological 10-m winds, lightly smoothed horizontal divergence, and SSTs from the Coupled Ocean Atmosphere Data Set (COADS) on a 2° $\times$ 2° grid. We use climatological July 850-mb temperature from the European Centre for Medium-Range Weather Forecasts (ECMWF) on a 5° $\times$ 5° grid. A constant lapse rate of 6 K km^{-1} is assumed between the inversion and 850 mb. Due to the paucity of soundings over this region, the ECMWF mixing ratio climatology is not used. Instead, a constant mixing ratio of 4 g kg^{-1} (Riehl et al. 1951; Minnis et al. 1992) is assumed between the inversion and the top of the domain at 1500 m, and a water vapor path of 5.7 kg m^{-2} above this level is used in the radiation calculations.

From the surface winds, we compute five trajectories starting at 40°N and a set of evenly spaced longitudes from 126° to 134° W (Fig. 15a). Also shown in Fig. 15a is the horizontal divergence, which is maximum just off the coast at 36°N. The SST and 850 hPa s^+/C_p are shown in Fig. 15b. The increase of s^+/C_p along each trajectory is much smaller than the increase of SST. We determine the time evolution of the environmental forcings input into the MLM on each of these trajectories using linear interpolation between the gridded data. Diurnally averaged insolation at the instantaneous trajectory latitude is used to remove the effects of diurnal decoupling. To crudely account for the systematic difference between the mean wind speed and the magnitude of the climatological mean wind vector, the wind speed V used in the MLM is chosen to be 1.2 times the magnitude of the COADS mean wind vector.

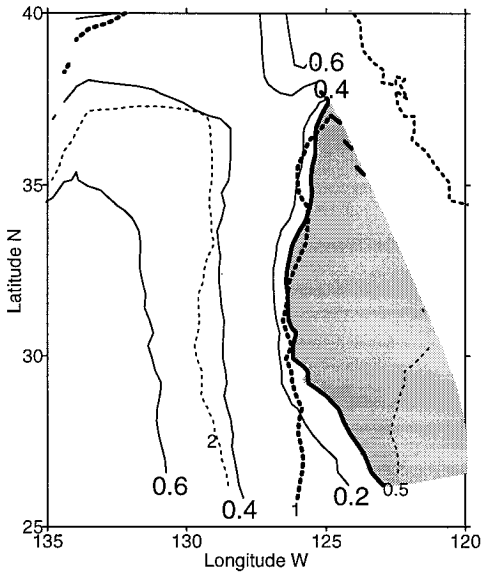

FIG. 15. (d) BIR (solid, 0.15 contour highlighted) and $\Delta F_R/QF_L(0)$ (dash, 1.0 contour highlighted). Shading indicates coupled CTBLs (BIR $<$ 0.15).

To initialize the MLM, a one-day back trajectory is

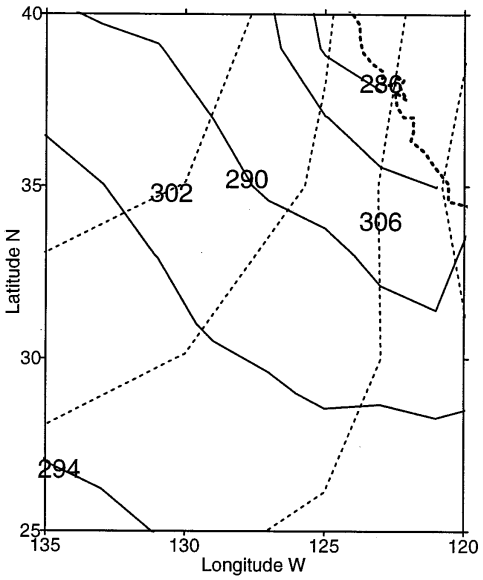

FIG. 15. (b) July climatological SST (solid) and s(850 hPa)/C_p (dash) in K.

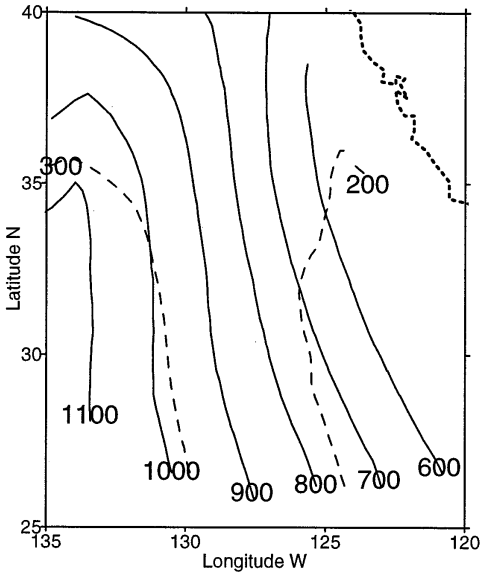

FIG. 15. (c) MLM inversion height (solid) and cloud thickness (dash) in m.

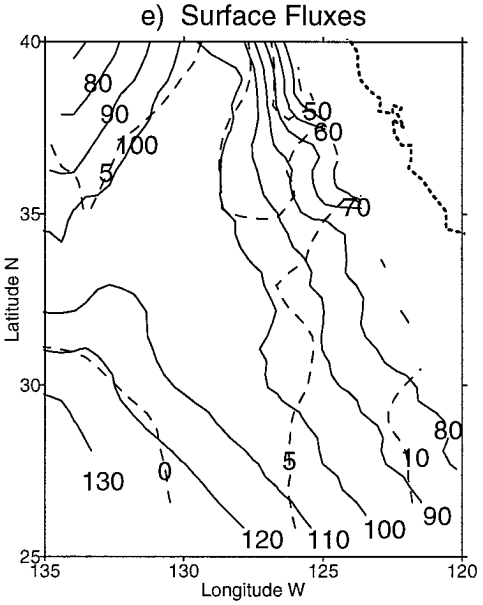

FIG. 15. (e) Surface latent (solid) and sensible (dash) heat fluxes in W m^{-2}.

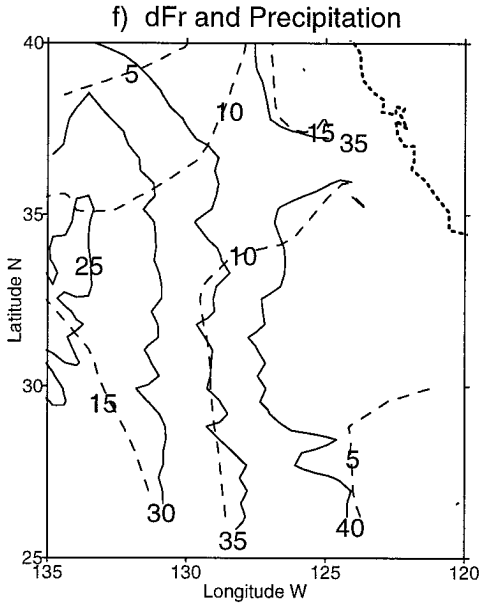

FIG. 15. (f) CTBL radiative flux divergence ΔF_R (solid) and scaled surface precipitation rate $-\rho_{ref}LF_P(0)$ (dash) in W m^{-2} (divide by 30 to obtain precipitation rate in mm day^{-1}).

calculated and the MLM is allowed to evolve for 1 day from the beginning of this back trajectory, with a starting inversion height of 650 m, a cloud thickness of 150 m, and an air–sea temperature difference of -0.5 K, to obtain a "day 0" initial state. Several other initialization procedures (including starting from a steady-state solution) were also tested. The solution depends somewhat on the initialization procedure during the first day of integration but becomes quite insensitive further along the trajectories. MLM-derived quantities calculated along these trajectories are interpolated to make regional contour maps.

The MLM inversion height and cloud thickness are shown in Fig. 15c, the BIR is shown in Fig. 15d, and the surface sensible and latent heat fluxes are shown in Fig. 15e. The cloud thickness varies from 150 m in the southeast corner to 350 m in the southwest. In general, the CTBL is deeper and more decoupled farther offshore. July mean low cloud cover varies between 0.6

and 0.8 over the entire oceanic region shown in the plots (and farther west out to 140°W), with the exception of a narrow strip of clearing near the coast (Betts et al. 1992). The MLM suggests that most of this area of persistent stratocumulus is associated with decoupled CTBLs. In the region where there is a downwind increase in SST, the decoupling threshold BIR = 0.15 corresponds fairly well to an inversion height of 700 m and a surface latent heat flux of 90 W m^{-2}.

The trajectory nearest the coast shows a slightly different evolution than the others, somewhat dependent on the initialization procedure. The inversion initially drops along a trajectory as divergence increases, then rises downstream. During the first day while the inversion is dropping, surface sensible heat fluxes are negative and the BIR exceeds 0.15. Downstream, the inversion remains shallow even as SST increases due to the strong divergence, and the BIR remains between 0 and 0.15, indicative of a coupled boundary layer.

Net radiative flux divergence ΔF_R across the CTBL and surface precipitation rate are shown in Fig. 15f. Both vary within comparable ranges to the control run. In Fig. 15d, we see that the simplified flux-ratio criterion $\Delta F_R/F_L(0) < Q$ (which ignores the contribution of drizzle) is generally a good predictor of regions that are decoupled (BIR > 0.15).

7. Conclusions

We have used a mixed-layer model to understand why stratocumulus-capped subtropical boundary layers tend to decouple as they advect over warmer water. We have also investigated the sensitivity of the boundary layer evolution and decoupling to the entrainment closure. We use solar radiative fluxes averaged over the entire diurnal cycle in our work; the deepening–warming decoupling discussed here is quite independent from diurnal decoupling. A similar downstream evolution is also seen in wintertime cold air outbreaks; in that case surface sensible heat fluxes play a more significant role but much of the analysis may still apply.

By examining the energy balance of the cloud-layer, we find that the entrainment rate, the cloud top and base and the latent heat fluxes are insensitive to the entrainment closure used. Small differences in the entrainment rate can create a sufficient range of buoyancy flux profiles to satisfy most entrainment closures.

Deepening-warming decoupling, on the other hand, is quite sensitive to the entrainment closure. We used the TN87 entrainment closure, which relates entrainment to turbulent eddy kinetic energy and inversion stratification. With this closure, decoupling is an inevitable consequence of the boundary layer changes that accompany an SST rise. The fundamental driving force for convection and entrainment is cloud layer diabatic cooling, which stays nearly constant as the SST warms. Thus, with the TN87 closure, the CTBL vertically average buoyancy fluxes, which determine the strength of the convective eddies, also do not change substantially as SST rises. However, the energy and moisture balance of the CTBL require a rapid increase in latent heat fluxes as SST rises. Strong latent heat fluxes force buoyancy fluxes to be much larger in the cloud layer than in the subcloud layer. To be consistent with the TN87 closure, in-cloud buoyancy fluxes rise but subcloud buoyancy fluxes become increasingly negative as SST rises, promoting decoupling.

One class of entrainment closures, ''flux-partitioning'' closures, determine entrainment rate by specifying how negative the subcloud buoyancy fluxes are. These closures by design cannot produce decoupling. A major uncertainty in the current study is that current observations and numerical simulations have not yet yielded a generally accepted entrainment parameterization for CTBLs. New observations and higher-resolution large-eddy simulation studies should help reduce this uncertainty in the next few years. As a first step in this direction, we have compared our MLM with W97's two-dimensional ERM simulations of CTBL evolution using the same boundary conditions. After minor modification of the MLM to better mimic the microphysics and inversion structure of the ERM, reasonable agreement was achieved. The deepening-warming decoupling found in the ERM had a very similar character and evolution to that predicted by the MLM.

We have found a ''minimal decoupling criterion'' for negative subcloud buoyancy fluxes: The ''flux ratio'' of boundary layer diabatic forcing to the surface latent heat flux must become smaller than a threshold value. The diabatic forcing is approximately the radiative flux divergence across the CTBL minus a ''drizzle'' term related to precipitation and evaporation. The threshold is proportional to (a) the fraction of the boundary layer filled by cloud and (b) the entrainment closure parameter *A*. For typical subtropical CTBLs, our criterion suggests that decoupling will occur once the surface latent heat fluxes exceed a threshold that is typically 50–100 W m^{-2}, depending on the environmental conditions. In our runs, drizzle promotes decoupling, but is not required to produce decoupling at SSTs of 290–295 K, characteristic of the warmer parts of the subtropical stratocumulus regimes.

A regional analysis using Lagrangian MLM simulations driven by July climatology for the northeastern Pacific Ocean suggests that most of the region of high stratocumulus cloud cover is associated with decoupled boundary layers; only the regions near the coast where SST is coldest, horizontal divergence is strongest, and boundary layer depths are less than 750 m are coupled in a diurnally averaged sense. Other subtropical stratocumulus regions are probably similar. The large expanses of subtropical stratocumulus in deeper boundary layers appear to form as a result of shallow cumulus detraining into a stratocumulus layer (Klein et al. 1995). Whether the much larger expanses of midlatitude oceanic stratocumulus (Klein and Hartmann 1993) also often lie atop decoupled boundary layers [as suggested by

work of Nicholls (1985) from the North Atlantic Ocean] remains an interesting and important question for a future observational study.

Because of deepening–warming decoupling, a physically based boundary layer parameterization must treat stratocumulus cloud amount due to both well-mixed and cumulus-coupled boundary layers as well as the transition between the two. In particular, it requires the integration of a cumulus parameterization, a cloud parameterization, and a turbulence parameterization that accurately represents layer cloud feedbacks on boundary turbulence. A few groups have introduced parameterizations of this type and used them to predict stratocumulus cloud cover (e.g., Wang 1993; Wang et al. 1993; Tiedtke 1993; Bechtold et al. 1992, 1995), with promising results. One element in the ultimate success of such parameterizations is a realistic depiction of decoupling. Decoupling does not immediately produce cloud breakup (W97). However, a boundary layer that is moistest near the surface will support a thinner cloud layer than a well-mixed boundary layer with the same mixing ratio, so we may expect decoupling to affect mean cloud albedo and the surface radiation balance.

Tiedtke's parameterization uses the depth of the conditionally unstable cloud layer as the principal predictor of decoupling, treating moist convection where conditional instability extends exactly one grid point above cloud base using a cloud-topped mixed-layer scheme and treating deeper convection using a cumulus scheme. Wang's parameterization also indirectly relates decoupling to the depth of the conditionally unstable cloud layer. In Wang's parameterization, the intensity of the updraft mass fluxes in the boundary layer is inversely related to the amount of conditional instability, favoring rapid turnover (well mixedness) in shallow boundary layers too shallow to allow much conditional instability. In Wang's model, both decoupling and cloud amount are quite sensitive to the parameterization of precipitation. Neither of these models appears to include a strong feedback of surface latent heat fluxes on decoupling. Bechtold et al.'s model, on the other hand, is based on turbulence closure and should directly simulate the decoupling process. Our work suggests this approach is more physically realistic. With continued efforts to compare simple models, operational parameterizations, large-eddy simulations, and observations, we should be able to make considerable further progress in representing decoupling and its consequences for stratocumulus cloudiness in global models.

Acknowledgments. This work was supported by ONR Grant N00014-90-J-1136, NASA Grant NAG1-1711, and an NSF Graduate Fellowship awarded to M. C. Wyant. Comments of Dr. Doug Lilly, Dr. Steve Krueger, and two anonymous reviewers substantially improved the manuscript.

APPENDIX A

Computation of w_e

Using (4)–(8), the buoyancy flux profile can be partitioned into a known component independent of entrainment (associated with the surface fluxes and the radiation and precipitation profiles) and a term proportional to the unknown entrainment rate:

$$\langle w'b' \rangle(z) = c_0(z) + c_1(z) w_e. \tag{A1}$$

At each grid point z_k, the formulas for $c_0(z_k)$ and $c_1(z_k)$ depend upon whether the grid point is saturated or not, due to the different formulas for buoyancy flux used in saturated versus unsaturated air. The saturated formulas for $c_0(z_k)$ and $c_1(z_k)$ are also computed for the grid point above cloud top so that the contribution to the buoyancy flux integral from above the highest in-cloud grid point can be included. Substitution of (A1) into (10) [using (13) to find A] determines w_e:

$$w_e = \alpha I_0/(1 - \sigma I_1), \tag{A2}$$

$$\alpha = 2.5 A s_{v0}/\{g z_i \Delta s_{vi}\}, \tag{A3}$$

$$I_j = \int_0^{z_i} dz\, c_j(z), \qquad j = 0, 1.$$

To find w_e, we must find I_0 and I_1. An accurate numerical approximation of these integrals, that accounts for the discontinuities in the c_j's at cloud base and top is crucial, else the cloud top does not evolve smoothly between grid levels. Let $I_j^{(k)}$ be the contribution to the integral I_j from $z_k < z < z_{k+1}$. The trapezoidal rule $I_j^{(k)} = 0.5\Delta z\{c_j(z_k) + c_j(z_{k+1})\}$ is used for the integration except near z_b and z_i. The discontinuities in c_j at z_i and z_b are handled by linear extrapolation of $c_j(z)$ out to the discontinuities to compute the integrals. Let *kb* and *ki* be the indices of the highest grid point below cloud base and the inversion, respectively, and let $f_b = (z_b/\Delta z - kb)$, $f_i = (z_i/\Delta z - ki)$, $g_b = 1 - f_b$, $g_i = 1 - f_i$. Then

$$I_j^{(kb)} = 0.5\Delta z\{-f_b{}^2 c_j(z_{kb-1}) + (2f_b + f_b{}^2)c_j(z_{kb}) + (2g_b + g_b{}^2)c_j(z_{kb+1}) - g_b{}^2 c_j(z_{kb+2})\},$$

$$I_j^{(ki)} = 0.5\Delta z\{(2f_i - f_i{}^2)c_j(z_{ki}) + f_i{}^2 c_j(z_{ki+1})\}.$$

APPENDIX B

Decoupling Threshold for MLM

To generalize criterion (22), we first construct the buoyancy flux profile given the surface fluxes $\langle w's_{vl}' \rangle(0)$ and $\langle w'q_t' \rangle(0)$, the precipitation flux profile $F_P(z)$, the normalized radiation flux $f_R(z) = F_R(z)/\rho_{\text{ref}}$, and the tendencies ds_{vlM}/dt and dq_{tM}/dt. We then apply the threshold condition that the subcloud buoyancy flux is zero to obtain $\langle w's_{vl}' \rangle(0)$ in terms of the other variables and use this buoyancy flux profile in the entrainment closure to find $w_e \Delta s_{vi}$ as in (20). We then generalize the energy

balance equation (21) to obtain a different expression for $w_e\Delta s_{vli}$. A comparison of these two expressions leads to our decoupling threshold.

From (8), the buoyancy flux profile is

$$\begin{aligned}\langle w's_v'\rangle(z) &= b_1(z)\langle w'h'\rangle(z) - b_2(z)L\langle w'q_t'\rangle(z)\\ &= b_1(z)\{E(z) - f_R(z)\} - b_2(z)L\{W(z) - F_P(z)\},\\ &= b_1(z)\{\langle w'h'\rangle(0) + f_R(0) - f_R(z) - zdh_M/dt\}\\ &\quad - b_2(z)L\{\langle w'q_t'\rangle(0) + F_p(0)\\ &\quad - F_P(z) - zdq_{tM}/dt\},\end{aligned}$$

$$b_1(z) = \begin{cases}1, & 0 < z < z_b\\ \beta, & z_b < z < z_i\end{cases}$$

$$b_2(z) = \begin{cases}1 - \delta\epsilon, & 0 < z < z_b\\ \epsilon, & z_b < z < z_i.\end{cases} \tag{B1}$$

From (B1), we can calculate w^{*3} and substitute into the entrainment closure as in (20). Denoting the vertical average of a quantity over the CTBL depth by an overbar and defining $a = 2.5A$, we find

$$\begin{aligned}w_e\Delta s_{vi} = T_1 = a[&\overline{b_1}\langle w'h'\rangle(0) + \overline{b_1(f_R(0) - f_R(z))}\\ &- \overline{b_1 z}\, dh_M/dt\\ &- L\{\overline{b_2}\langle w'q_t'\rangle(0) + \overline{b^2(F_{P(0)} - F_P(z))}\\ &- \overline{b_2 z}\, dq_{tM}/dt\}].\end{aligned} \tag{B2}$$

We can also find a generalization of the energy balance Eq. (21) using (2)–(7):

$$\begin{aligned}w_e\Delta s_{vli} = T_2 = &-\langle w'h'\rangle(0) + \mu L\langle w'q_t'\rangle(0) + f_R(z_i)\\ &- f_R(0) + \mu LF_p(0) + z_i ds_{vl}/dt.\end{aligned} \tag{B3}$$

Now $\Delta s_{vi} = \Delta s_{vli} - (\mu - \epsilon)Lq_{\rm li}$, where $q_{\rm li}$ is the liquid water mixing ratio just below the inversion, so

$$T_1 - T_2 + (\mu - \epsilon)w_e Lq_{\rm li} = 0. \tag{B4}$$

From (B1), the threshold of zero subcloud buoyancy flux requires that

$$\begin{aligned}\langle w's_v'\rangle(z_b^-) &= 0\\ &= \langle w'h'\rangle(0) - \mu L\{\langle w'q_t'\rangle(0)\\ &\qquad + f_R(0) - f_R(z_i^-)\\ &\qquad - z_b\, dh_M/dt\}\\ &\quad - \mu L\{F_P(0) - F_P(z_b) - z_b dq_{tM}/dt\}.\end{aligned} \tag{B5}$$

Using (B5) to eliminate $\langle w'h'\rangle(0)$ from (B4), we obtain the threshold condition (24), where

$$k_v = \rho_{\rm ref}\{a\overline{b_1 z} + z_i - [1 - a\overline{b_1}]z_b\}, \tag{B6}$$

$$k_r = \rho_{\rm ref}aL\overline{(b_2 - \mu b_1)z}, \tag{B7}$$

$$\begin{aligned}S_R = &\ a\overline{b_1[F_R(0) - F_R(z)]}\\ &- [1 + a\overline{b_1}][F_R(0) - F_R(z_b)],\end{aligned} \tag{B8}$$

$$\begin{aligned}S_P = &-\rho_{\rm ref}L\{a\overline{b_2[F_P(0) - F_P(z)]} + \mu F_D(0)\\ &- \mu[1 + a\overline{b_1}][F_P(0) - F_P(z_b)]\},\end{aligned} \tag{B9}$$

$$S_C = \rho_{\rm ref}L(\mu - \epsilon)w_e q_{\rm li}. \tag{B10}$$

REFERENCES

Albrecht, B. A., D. A. Randall, and S. Nicholls, 1988: Observations of marine stratocumulus during FIRE. *Bull. Amer. Meteor. Soc.*, **69,** 619–626.

——, C. S. Bretherton, D. Johnson, W. Schubert, and A. S. Frisch, 1995a: The Atlantic Stratocumulus Transition Experiment (ASTEX). *Bull. Amer. Meteor. Soc.*, **76,** 889–903.

——, M. P. Jensen, and W. J. Syrett, 1995b: Marine boundary layer structure and fractional cloudiness. *J. Geophys. Res.*, **100,** 14 209–14 222.

Bechtold, P., C. Fravalo, and J.-P. Pinto, 1992: A model of marine boundary layer cloudiness for mesoscale applications. *J. Atmos. Sci.*, **49,** 1723–1744.

——, J. W. M. Cuijpers, P. Mascart, and P. Trouilhet, 1995: Modeling of trade wind cumuli with a low-order turbulence model: Toward a unified description of Cu and Sc clouds in meteorological models. *J. Atmos. Sci.*, **52,** 1723–1744.

Betts, A. K., P. Minnis, W. Ridgway, and D. F. Young, 1992: Integration of satellite and surface data using a radiative-convective oceanic boundary-layer model. *J. Appl. Meteor.*, **31,** 340–350.

Bougeault, P., 1985: The diurnal cycle of the marine stratocumulus layer: A higher-order model study. *J. Atmos. Sci.*, **42,** 2826–2843.

Bretherton, C. S., 1992: A conceptual model of the stratus-trade cumulus transition in the subtropical oceans. *Proc. 11th Int. Conf. on Clouds and Precipitation*, Vol. 1, Montreal, PQ, Canada, Int. Comm. on Clouds and Precip. and Int. Assoc. Meteor. Atmos. Physics, 374–377.

——, P. Austin, and S. T. Siems, 1995: Cloudiness and marine boundary layer dynamics in the ASTEX Lagrangian experiments. Part II: Cloudiness, drizzle, surface fluxes and entrainment. *J. Atmos. Sci.*, **52,** 2724–2735.

Deardorff, J. W., 1976: on the entrainment rate of a stratocumulus-capped mixed layer. *Quart. J. Roy. Meteor. Soc.*,**102,** 563–582.

Duynkerke, P. G., 1993: Simulation of diurnal variation in a stratocumulus-capped marine boundary layer during FIRE. *Mon. Wea. Rev.*, **121,** 3291–3300.

Hignett, P., 1991: Observations of diurnal variation in a cloud-capped marine boundary layer. *J. Atmos. Sci.*, **48,** 1474–1482.

Klein, S. A., and D. L. Hartmann, 1993: The seasonal cycle of low stratiform clouds. *J. Climate*, **6,** 1587–1606.

——, D. L. Hartmann, and J. R. Norris, 1995: On the relationships among low-cloud structure, sea-surface temperature and atmospheric circulations in the summertime northeast Pacific. *J. Climate*, **8,** 1140–1155.

Kraus, H., and E. Schaller, 1978: A note on the closure in Lilly-type inversion models. *Tellus*, **30,** 284–288.

Krueger, S. K., G. T. McLean, and Q. Fu, 1995: Numerical simulations of the stratus to cumulus transition in the subtropical marine boundary layer. Part I: Boundary layer structure. *J. Atmos. Sci.*, **52,** 2839–2850.

Lewellen, D. C., W. S. Lewellen, and S. Yoh, 1996: Influence of Bowen ratio on boundary layer cloud structure. *J. Atmos. Sci.*, **53,** 175–187.

Lilly, D. K., 1968: Models of cloud-topped mixed layers under a strong inversion. *Quart. J. Roy. Meteor. Soc.,* **94,** 292–309.
McEwan, A. D., and G. W. Paltridge, 1976: Radiatively driven thermal convection bounded by an inversion—A laboratory simulation of stratus clouds. *J. Geophys. Res.,* **81,** 1095–1102.
Minnis, P., P. W. Heck, and D. F. Young, 1992: Stratocumulus cloud properties derived from simultaneous satellite and island-based instrumentation during FIRE. *J. Appl. Meteor.,* **31,** 317–339.
Moeng, C.-H., 1986: Large-eddy simulation of a stratus-topped boundary layer. Part I: Structure and budgets. *J. Atmos. Sci.,* **43,** 2886–2900.
Moyer, K., and G. Young, 1993: Buoyant forcing within the marine stratocumulus-topped boundary layer. *J. Atmos. Sci.,* **50,** 2759–2771.
Neiburger, M., 1960: Studies of airmass structure to the field of motion over the eastern north Pacific Ocean in summer. *Tellus,* **12,** 31–40.
Nicholls, S., 1984: The dynamics of stratocumulus: Aircraft observations and comparisons with a mixed layer model. *Quart. J. Roy. Meteor. Soc.,* **110,** 783–820.
——, 1985: Aircraft observations of the Ekman layer during the Joint Air–Sea Interaction Experiment. *Quart. J. Roy. Meteor. Soc.,* **111,** 391–426.
——, and J. Leighton, 1986: An observational study of the structure of stratiform cloud layers. Part I. Structure. *Quart. J. Roy. Meteor. Soc.,* **112,** 431–460.
——, and J. D. Turton, 1986: An observational study of the structure of stratiform cloud layers. Part II. Entrainment. *Quart. J. Roy. Meteor. Soc.,* **112,** 461–480.
Randall, D. A., 1980: Conditional instability of the first kind upside-down. *J. Atmos. Sci.,* **37,** 125–130.
Riehl, H., T. C. Yeh, J. S. Malkus, and N. E. LaSeur, 1951: The northeast trade of the Pacific Ocean. *Quart. J. Roy. Meteor. Soc,* **77,** 598–626.
Schubert, W. H., J. S. Wakefield, E. J. Steiner, and S. K. Cox, 1979: Marine stratocumulus convection. Part I: Governing equations and horizontally homogeneous solutions. *J. Atmos. Sci.,* **36,** 1286–1307.
Tiedtke, M., 1993: Representation of clouds in large-scale models. *Mon. Wea. Rev.,* **121,** 3040–3061.
Turton, J. D., and S. Nicholls, 1987: Diurnal variation of stratocumulus. *Quart. J. Roy. Meteor. Soc.,* **113,** 969–1009.
Wakefield, J. S., and W. H. Schubert, 1981: Mixed-layer model simulation of eastern North Pacific stratocumulus. *Mon. Wea. Rev.,* **109,** 1952–1968.
Wang, S., 1993: Modeling marine boundary-layer clouds with a two-layer model: A one-dimensional simulation. *J. Atmos. Sci,* **50,** 4001–4021.
——, B. A. Albrecht, and P. Minnis, 1993: A regional model of marine boundary layer clouds. *J. Atmos. Sci.,* **50,** 4022–4043.
Wyant, M. C., C. S. Bretherton, H. A. Rand, and D. E. Stevens, 1997: Numerical simulations and a conceptual model of the subtropical marine stratocumulus to trade cumulus transition. *J. Atmos. Sci.,* **54,** 168–192.